AI-Enhanced Pilot-Assisted Angle-of-Arrival Estimation for Wearable Devices in Rician Fading Channels: A Low-SNR Focused Method

IEEE Access
Multidisciplinary ⋮ Rapid Review ⋮ Open Access Journal

Received 22 October 2025, accepted 9 November 2025, date of publication 18 November 2025,
date of current version 25 November 2025.

Digital Object Identifier 10.1109/ACCESS.2025.3634289

RESEARCH ARTICLE

AI-Enhanced Pilot-Assisted Angle-of-Arrival Estimation for Wearable Devices in Rician Fading Channels: A Low-SNR Focused Method

AHMAD ALDELEMY[1], (Member, IEEE), ALI AL-DULAIMI[2], (Member, IEEE), GEILI T. A. EL SANOUSI[3,4], (Member, IEEE), PRINCE O. SIAW[1], (Member, IEEE), NAZAR T. ALI[5], (Senior Member, IEEE), VIKTOR DOYCHINOV[1], (Senior Member, IEEE), YOUSEF DAMA[6], (Senior Member, IEEE), AND RAED A. ABD-ALHAMEED[1,7], (Senior Member, IEEE)

[1]Faculty of Engineering and Digital Technologies, University of Bradford, BD7 1DP Bradford, U.K.
[2]School of Computing and Innovative Technologies, British University Vietnam (BUV), Hanoi 160000, Vietnam
[3]Department of Design Engineering, Faculty of Technology, Middlesex University London, NW4 4BT London, U.K.
[4]Faculty of Engineering, Electrical Engineering Department, Omdurman Ahlia University, Omdurman 50728, Sudan
[5]Department of Electrical Engineering and Computer Science, Khalifa University, Abu Dhabi, United Arab Emirates
[6]Department of Electrical and Computer Engineering, An-Najah National University, Nablus P411 0257, Palestine
[7]Department of Information and Communication Engineering, Al-Farqadin University College, Basrah 61004, Iraq

Corresponding author: Raed A. Abd-Alhameed (r.a.a.abd@bradford.ac.uk)

This work was supported in part by the U.K. Engineering and Physical Sciences Research Council (EPSRC) under Grant EP/X039366/1; and in part by the HORIZON-MSCA-RISE, a Marie Skłodowska-Curie Research and Innovation Staff Exchange (RISE) Initiative titled "FractuRe Orthopaedic Rehabilitation: Ubiquitous eHealth Solution (Robust)," under Project 101086492.

ABSTRACT Accurate angle-of-arrival (AoA) estimation is critical for precise localisation in wearable devices, particularly in challenging wireless environments such as Rician fading with low signal-to-noise ratios (SNRs). This paper proposes a pilot-assisted AoA estimation technique that integrates pseudo-random permutations and Walsh sequences within an OFDM-based transmission framework. The method preserves phase coherence and enhances spatial resolution by optimising pilot allocation and leveraging advanced signal processing. Comprehensive MATLAB simulations show high robustness: At -38 dB (per-subcarrier, per-snapshot SNR), the $\approx 1.5°$ RMS is achieved by aggregating across L snapshots and multiple subcarriers (see Table 12 for K-factor scenarios), with sub-degree accuracy at moderate-to-high SNRs. Furthermore, a lightweight, one-dimensional (1D) convolutional neural network (CNN) reduces residual carrier-frequency offsets by over 30%, highlighting a promising synergy between classical signal processing and data-driven learning. Comparative analysis against state-of-the-art techniques and a discussion of computational complexity are provided, underscoring the suitability of the proposed method for next-generation wearable and IoT direction-finding applications.

INDEX TERMS Angle-of-arrival (AoA) estimation, wearable devices, Rician fading channels, orthogonal frequency-division multiplexing (OFDM), pilot-assisted direction finding, Walsh sequences.

I. INTRODUCTION

Accurate angle-of-arrival (AoA) estimation underpins numerous emerging services in wearable technology, from advanced healthcare monitoring and sports performance analytics to safety, navigation, and security applications. For instance, precise AoA measurements can enhance indoor navigation in hospitals, assist in athlete tracking for training optimisation, or guide emergency responders in locating victims within cluttered indoor environments. As wearable devices proliferate daily, these systems must operate robustly in dynamic multipath conditions where

The associate editor coordinating the review of this manuscript and approving it for publication was Yi Ren.

multipath fading, noise, and non-line-of-sight (NLOS) paths introduce significant challenges.

Current approaches often struggle in low signal-to-noise ratio (SNR) regimes and complex Rician channel conditions, limiting the achievable localisation accuracy. Conventional orthogonal frequency division multiplexing (OFDM)-based solutions, while effective for data transmission, may fail to maintain stable phase references critical for AoA tasks. This creates a clear research gap: a dedicated AoA-oriented technique that can reliably extract coherent angular information even when pilot counts are limited and frequency offsets are non-negligible.

The proposed technique addresses this gap by integrating pilot-assisted OFDM, pseudo-random permutations, and Walsh sequences to refine phase references and leverage controlled pilot distributions. This AoA-centric strategy focuses on angle accuracy over general link metrics, enabling improved positioning capabilities for next-generation wearable communication systems. The practical necessity of a robust AoA estimation method is underscored by previous studies that highlight its crucial role in healthcare [1], indoor navigation [2], [3], and IoT/wearable networks [4].

This research introduces a tailored AoA estimation method that integrates pilot signals, pseudo-random permutations, and Walsh sequences within an OFDM framework. By emphasising AoA accuracy, the technique refines phase references and leverages controlled pilot distributions to minimise angle errors. The result is a robust and flexible AoA estimation strategy that significantly enhances directional precision in wearable scenarios, enabling improved positioning capabilities for next-generation wearable communication systems.

Accurate positioning is essential in numerous wearable-device applications, necessitating the development of effective techniques for extracting directional information [1], [3]. Because antenna arrays and space-modulation approaches enhance the ability to discriminate incoming signals' directions, AoA estimation remains among the most promising solutions to improve localisation accuracy in body-centric or wearable scenarios. However, body movements, multipath fading, and low-SNR conditions introduce significant challenges [5], [6], [7], [8], [9]. Wearable nodes often transmit at reduced power levels to conserve energy, resulting in an SNR of less than 0 dB [10]. Partial or complete signal obstruction by the human body further adds absorption and scattering effects, degrading the received signal's quality [5].

To address these constraints, a variety of robust algorithms have emerged, including subspace-based methods like MUSIC/ESPRIT and machine-learning estimators, aiming to preserve reliable performance both in controlled tests [11], [12], [13], [14] and real-world setups [15], [16]. Collectively, such works confirm that wearable and body-centric devices must adopt specialised AoA estimation techniques that handle negative-SNR, body-induced attenuation, and frequent motion.

In OFDM systems, pilot assistance has proven indispensable for mitigating frequency selectivity, especially when subcarriers undergo deep fades [14], [15], [16], [17]. A series of studies highlights optimised pilot-symbol design or preamble-based approaches that minimise mean-squared error in channel estimation [18], [19]. For instance, pilot signals can be allocated strategically in systems with null subcarriers to counteract channel nulls, ensuring robust channel recovery under multipath [18]. Moreover, adaptive interpolation methods enhance coherent detection when facing doubly selective Rayleigh fading, underlining that properly chosen pilot patterns significantly boost signal integrity [18].

This aligns with earlier work suggesting that pilot recruitment strategies can reduce angular error and reinforce reliability in wearable wireless systems [20], [21]. Pilot-aided OFDM remains a key challenge in high-mobility scenarios where time and frequency selectivity intersect, yet such pilot-based solutions strongly enhance channel estimation, data fidelity, and, ultimately, AoA performance.

Accurate channel modelling is essential for capturing the interplay of direct paths and scattered reflections in wearable systems. Rician fading is widely deemed the best fit in these contexts due to partial line-of-sight dominance plus weaker diffuse scattering [5], [15], [22], [23], [24]. Multipath-rich indoor settings, such as clinics or gyms, add further complexity, with signals bouncing off reflective surfaces [25]. Past research also emphasises the importance of subspace-based methods adapted to wideband or ultra-wideband signals [26], in conjunction with Rician modelling, for effective direction-finding. Consequently, thorough channel analysis, covering both direct and scattered components, proves critical in designing wearable antenna layouts and AoA signal-processing methods [15], [23].

Although this study primarily focuses on OFDM, related works often target Orthogonal Frequency-Division Multiple Access (OFDMA) due to its wide adoption in modern communication systems. However, the proposed study demonstrates the potential for adaptation to both OFDM and OFDMA environments. In both cases, frequency-offset estimation remains a major concern for subcarrier orthogonality, as even small offsets can significantly degrade system performance. Existing literature derives maximum-likelihood Carrier Frequency Offset (CFO) estimators that incorporate pilot signals for reliable synchronisation [27], [28]. Even modest offsets can degrade the received signal's phase continuity, thus confounding AoA measurements. Further investigations show how offset errors in channel-sounding or MIMO systems bias AoA estimation, underlining the necessity of precise CFO correction [29], [30].

By merging contributions and findings, the paper offers a comprehensive overview of an innovative AoA estimation method to enhance wearable communication systems in noisy, multipath-rich scenarios. The paper is organised as follows: Section II introduces the underlying principles;

TABLE 1. Global notation used throughout the paper (unified).

Symbol	Meaning
M	Number of array elements (antennas)
N	FFT length (number of subcarriers)
N_{used}	Number of *active* subcarriers
N_p	Number of pilot subcarriers per OFDM symbol
$\rho_{\text{pilot}} \triangleq N_p/N_{\text{used}}$	Pilot fraction (overhead)
L	Snapshots (OFDM symbols) used in statistics
B	Occupied bandwidth
$\Delta f = B/N$	Subcarrier spacing
$\lambda = c/f_c$, d	Wavelength and inter-element spacing
ϵ, μ, ξ	Fractional, integer, and total normalised CFO ($\xi = \mu + \epsilon$)
SNR	Per-subcarrier, per-snapshot unless stated otherwise
ε	Per-trial angular error ($\phi_{est} - \phi_{true}$)
Mean Error	Average of ε over trials
RMS Error	Root Mean Square of ε over trials
SD	Standard Deviation of ε over trials
CDF(x)	Cumulative Distribution Function, $P(\lvert\varepsilon\rvert \leq x)$

Section III describes the methodology and simulation framework; Section IV presents the results and technical analysis, including dedicated validation in ultra-dense multipath conditions and an evaluation of an AI-enhanced correction model; and Section V discusses the findings, summarises the key results, highlights limitations, and suggests future research.

II. THEORETICAL BACKGROUND AND CONCEPTUAL FRAMEWORK

Wearable devices increasingly operate in dynamic, multipath-rich, and low-SNR environments where traditional Angle-of-Arrival (AoA) estimation methods fail to deliver the required accuracy. Challenges such as frequency offsets, multipath fading, channel distortions, and dynamic user motion significantly hinder the extraction of stable phase information, especially in low-power, bandwidth-constrained systems. These limitations are particularly acute in wearable technologies, where precise localisation is essential for applications such as healthcare monitoring, fitness tracking, and emergency response [1], [2].

Conventional Orthogonal Frequency Division Multiplexing (OFDM)-based solutions, while effective for data transmission, often fail to meet the demands of accurate AoA estimation. Inter-carrier interference, high peak-to-average power ratios, and frequency synchronisation issues degrade angular precision [3], [4]. Furthermore, such solutions frequently focus on general link metrics rather than angular accuracy, making them suboptimal for scenarios where directional precision is critical, such as body-centric communications and wearable networks [5].

To address these challenges, this work introduces a novel AoA estimation framework tailored for wearable devices operating in Rician fading channels. The proposed method integrates:

- **Pilot-assisted OFDM configurations** to enhance phase coherence and spatial resolution.
- **Walsh sequences** and **pseudo-random permutations** to optimise coding schemes, ensuring stable phase relationships under multipath conditions.
- **Direction-finding-centric metrics** that prioritise angular precision over general transmission performance.

These elements collectively enable reliable AoA estimation in scenarios characterised by negative SNR values, constrained pilot resources, and high-frequency offsets.

The motivation for prioritising AoA estimation stems from the growing reliance on wearable technologies in applications requiring precise direction-finding capabilities. For instance, healthcare systems depend on accurate localisation for patient monitoring and asset tracking in hospitals, while security wearables facilitate the real-time positioning of emergency responders in complex indoor environments [6], [7]. Moreover, AoA estimation plays a pivotal role in the broader context of the Internet of Wearable Devices (IoWD), a critical subset of the Internet of Everything (IoET), where device coordination, interference management, and spatial awareness are indispensable [8].

Unlike conventional solutions that assume stable propagation conditions and high power levels, this framework is designed specifically for wearable scenarios, where body-induced attenuation, dynamic motion, and multipath propagation dominate. By leveraging robust pilot configurations and coding techniques, the proposed approach achieves sub-degree AoA accuracy at moderate-to-high SNR while remaining robust at low SNR (e.g., RMS $\approx 1.5^\circ$ at -38 dB).

In summary, this research advances AoA estimation by:

- Overcoming the limitations of conventional OFDM systems through direction-finding-centric designs, leveraging pilot configurations and Walsh sequences for enhanced precision.
- Achieving robust angular precision in wearable and body-centric communications, with demonstrated performance in low-SNR environments.
- Highlighting potential applicability across diverse use cases, including healthcare asset tracking, fitness navigation, and emergency response.

Through these contributions, this work establishes a new benchmark for integrating reliable AoA estimation into wearable technologies, enhancing both individual device functionality and the broader ecosystem of body-centric communication systems.

III. METHODOLOGY AND SIMULATION FRAMEWORK

This section details the proposed pilot-assisted AoA estimation framework, beginning with an overview of the OFDM signal model and concluding with the statistical validation approach. The methodology is designed to achieve robust performance in low-SNR, Rician fading environments typical of wearable device operation. While our framework is fundamentally pilot-assisted, it leverages spatial covariance

processing techniques, conceptually related to subspace methods, to achieve its high resolution without requiring a full eigendecomposition.

A. SYSTEM MODEL AND PARAMETERS

The proposed Angle-of-Arrival (AoA) estimation framework is designed to address the challenges of wearable communication systems, including limited power, restricted bandwidth, and dynamic multipath fading. This section outlines the system model, key parameters, and simulation setup, ensuring a balance between spectral efficiency and AoA resolution.

1) SYSTEM OVERVIEW

The framework is based on an Orthogonal Frequency Division Multiplexing (OFDM) transmission scheme, which is well-suited for high-data-rate communication in multipath environments. An antenna array with a carefully designed geometry is employed to achieve high spatial resolution for AoA estimation. A Rician fading channel model is utilised to emulate realistic wearable scenarios, where a dominant Line-of-Sight (LOS) path coexists with scattered Non-Line-of-Sight (NLOS) components. The simulation framework is divided into five main stages:

1) **Parameter Configuration:** Define key system parameters and simulation settings.
2) **Antenna Array Design:** Configure the antenna array geometry for optimal spatial resolution.
3) **Channel Simulation:** Model the Rician fading channel with realistic multipath effects.
4) **Frequency Offset Correction:** Estimate and correct frequency offsets to maintain phase coherence.
5) **AoA Extraction:** Extract the angle of arrival from the processed channel response.

The workflow, summarised in Figure 1, is structured into these five distinct stages. The following sections detail the signal representation and processing steps.

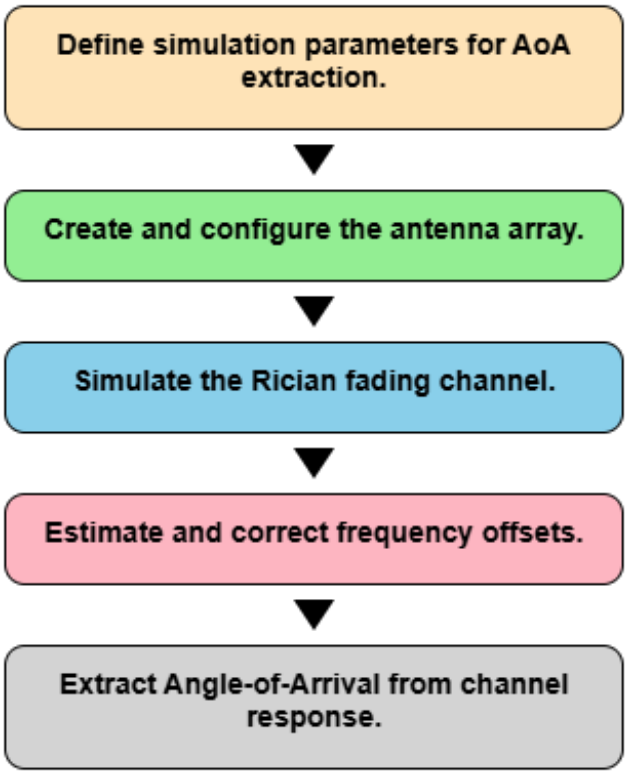

FIGURE 1. Simplified simulation flow summarising the critical steps involved in AoA estimation.

a: OFDM BASEBAND SIGNAL REPRESENTATION

Since we employ an N-subcarrier OFDM scheme, the time-domain baseband signal for a single OFDM symbol can be represented as:

$$s(n) = \frac{1}{\sqrt{N}} \sum_{k=0}^{N-1} X(k)\, \exp\left(j 2\pi \frac{k}{N} n\right), \quad n = 0, \ldots, N-1, \tag{1}$$

where $X(k)$ is the frequency-domain symbol (pilot or data) mapped onto the k-th subcarrier, and $j = \sqrt{-1}$. The factor $1/\sqrt{N}$ ensures normalisation. In subsequent sections, we detail how pilot subcarriers and geometric considerations enable robust AoA estimation under Rician fading conditions [31].

b: IFFT AT THE TRANSMITTER

For clarity, the OFDM generation at the transmitter can also be described by the inverse Fourier transform:

$$x(n) = \frac{1}{\sqrt{N}} \sum_{k=0}^{N-1} X(k)\, \exp\left(j \frac{2\pi}{N} k\, n\right), \quad n = 0, 1, \ldots, N-1, \tag{2}$$

which is mathematically equivalent to (1). Here, $x(n)$ is the discrete-time waveform of the N-sample OFDM symbol before adding the cyclic prefix.

2) KEY PARAMETERS

The system's performance is governed by several critical parameters, carefully selected to balance spectral efficiency, AoA resolution, and computational complexity. These parameters include:

- **Carrier Frequency** (f)**:** 400 MHz, chosen to achieve a wavelength (λ) of approximately 0.7495 m, enabling antenna elements to be spaced at $\lambda/2$ intervals to mitigate spatial aliasing.
- **Bandwidth** (B)**:** 5 MHz, selected to provide sufficient spectral resources for accurate channel estimation while maintaining low power consumption.
- **FFT Length** (N)**:** Determines the number of subcarriers, impacting the system's spectral efficiency and

resolution. The subcarrier spacing is

$$\Delta f = \frac{B}{N},$$

which in turn sets the OFDM symbol duration

$$T_{\text{OFDM}} = \frac{1}{\Delta f} = \frac{N}{B}.$$

- **Cyclic Prefix (CP) Duration:** Chosen to mitigate inter-symbol interference (ISI) caused by multipath propagation. Typically,

$$T_{\text{CP}} \geq \tau_{\max},$$

where $\tau_{\max}$ is the maximum excess delay (or ''tap length'') expected in the channel.
- **Tap Length:** Set to 64, representing the length of the channel impulse response in the time domain.

The relationship between these parameters is critical for achieving high-resolution AoA estimation. For example, the wavelength λ is calculated as

$$\lambda = \frac{c}{f} = \frac{2.998 \times 10^8}{400 \times 10^6} = 0.7495 \text{ metres},$$

where c is the speed of light. This wavelength allows antenna elements to be spaced at $\lambda/2 \approx 0.37475$ metres, ensuring distinct phase observations for accurate AoA estimation. Meanwhile, the chosen FFT length N and bandwidth B set the subcarrier spacing Δf, which influences the available resolution in both frequency and time domains, directly affecting channel estimation accuracy and, ultimately, AoA precision.

3) SIMULATION SETUP

The simulation framework is organized into a modular architecture, with each module focusing on a specific aspect of the AoA estimation process. This structured approach ensures clarity, scalability, and reproducibility, enabling the simulation to accurately emulate real-world wearable communication scenarios. The simulation begins with the generation of input data symbols and pilot patterns, which are configured according to the chosen OFDM parameters. Pilot signals are strategically inserted using pseudo-random permutations and Walsh sequences to establish stable phase references and facilitate precise channel estimation.

Once the OFDM frames are generated, the simulation introduces the Rician fading channel, which is parametrised with specific Line-of-Sight (LOS) angles, K-factors, and scattering distributions to emulate realistic multipath environments. Noise and frequency offsets, representing hardware imperfections and Doppler shifts caused by user mobility, are added to simulate the challenging conditions typical of wearable communication systems. The simulation then proceeds to frequency-offset estimation and compensation, followed by channel estimation and AoA extraction.

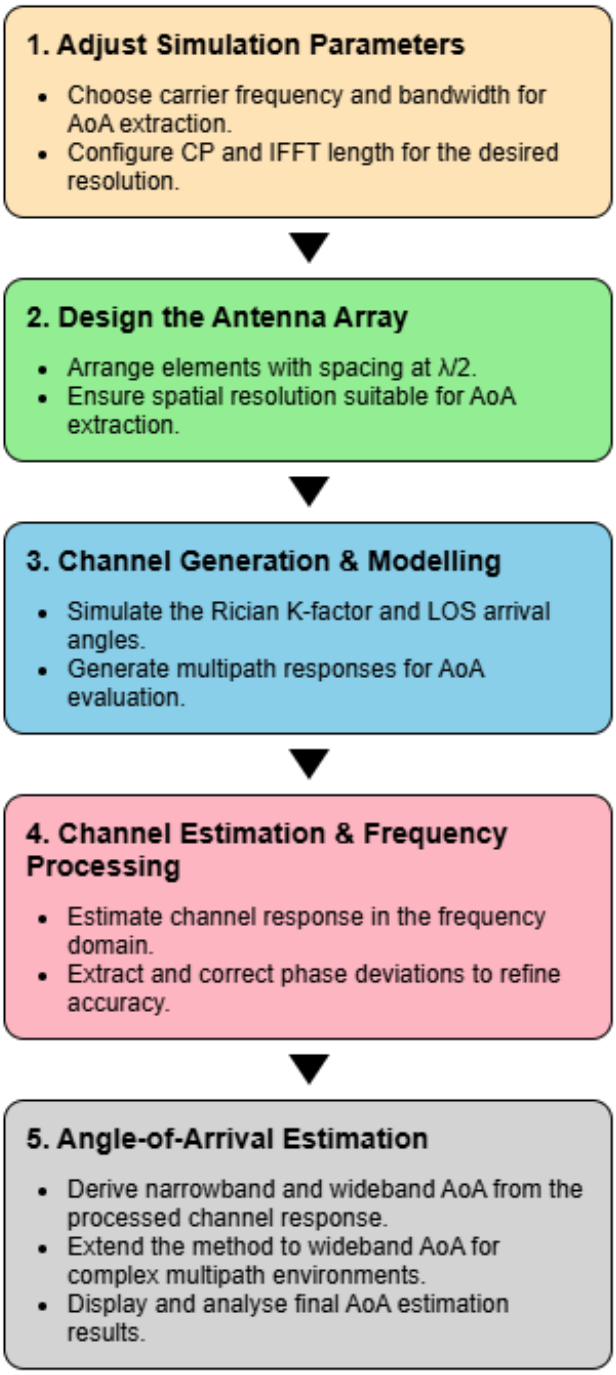

FIGURE 2. Detailed simulation pipeline illustrating the five main stages of AoA estimation.

4) SIMULATION FLOW

The simplified flowchart introduced earlier (Figure 1) provided an initial overview. In contrast, the detailed pipeline shown in Figure 2 visually represents the five main stages of the simulation flow, providing a concise snapshot of the core processes involved. The focus here is on the more comprehensive breakdown of each stage:

- **Define Simulation Parameters:** Key parameters such as FFT length, bandwidth, and carrier frequency are

TABLE 2. Simulation parameters used for AoA estimation.

Parameter Name	Definition	Value
c	Speed of light (m/s)	2.998×10^8
f	Carrier frequency (Hz)	400×10^6
λ	Wavelength (c/f) (m)	0.7495
B	Bandwidth (Hz)	5×10^6
Tap Length	Channel impulse response length	64

configured to balance spectral efficiency with AoA accuracy.

- **Antenna Array Design:** The array configuration, including element spacing and geometry, is optimized to mitigate spatial aliasing and enhance resolution.
- **Channel Simulation:** The Rician fading model is employed to emulate realistic multipath environments, ensuring robustness in wearable scenarios.
- **Frequency Offset Correction:** Integer and fractional offsets are estimated and corrected to ensure stability in AoA estimation.
- **AoA Extraction:** The processed channel response is used to estimate the AoA through established algorithms, providing accurate results under various signal and noise conditions.

5) PARAMETER SUMMARY

Table 1 summarizes the key simulation parameters and their values, providing a concise reference for the system's configuration.

These parameters enable spatial sampling by spacing antenna elements at approximately $\lambda/2$, mitigating spatial aliasing and preserving angular information critical for accurate AoA estimation. By balancing these parameters, the simulation ensures spectral efficiency while maintaining high-resolution AoA capabilities, even under wearable-specific constraints.

B. ANTENNA ARRAY CONFIGURATION

Accurate AoA estimation relies on the spatial sampling of incoming wavefronts by an antenna array. The simulation defines a specific geometry, typically comprising a small set of elements spaced at approximately $\lambda/2$. This spacing ensures sufficient angular resolution and avoids spatial aliasing, which is critical for accurate angle extraction [32].

These coordinates are integrated into the channel modelling process, ensuring that each antenna element receives unique phase and amplitude profiles. This approach preserves the angular information embedded in the channel and allows precise AoA estimation. By establishing the antenna layout early on, the framework guarantees that all frequency-domain processing and time-domain transformations encode the necessary spatial information effectively.

The array response vector $\mathbf{a}(\varphi)$ describes the phase relationships for a narrowband plane wave impinging from azimuth φ. We assume a ULA oriented along the x-axis with element positions $\mathbf{r}_m = ((m-1)d,\ 0,\ 0)^\top, m = 1, \ldots, M$.

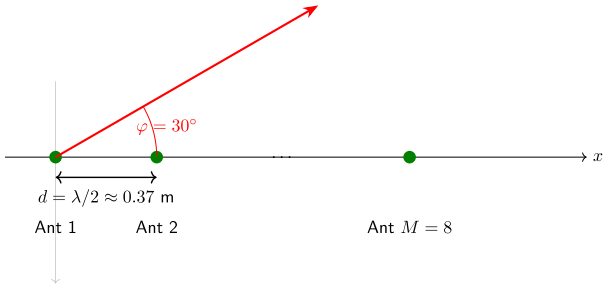

FIGURE 3. Uniform linear array (ULA) with $M = 8$ elements and inter-element spacing $d = \lambda/2 = 0.37475$ m at $f_c = 400$ MHz; illustrated arrival azimuth $\varphi = 30°$. Baseline results use CM: off (see Sec. III-B-I). *(Scope note.)* For on-body prototypes, physical aperture scales with d/λ; at higher f_c (e.g., 2.4 GHz) the same M and d/λ imply an ≈ 6× smaller aperture.

Notation: We use the unit direction vector $\hat{\mathbf{k}} = [\cos\varphi,\ \sin\varphi,\ 0]^\top$ and write the m-th element response as

$$a_m(\varphi) = \exp\Big(j\,\frac{2\pi}{\lambda}\,\hat{\mathbf{k}}^\top \mathbf{r}_m\Big),$$

so the factor $2\pi/\lambda$ appears exactly once [33]. The full response vector is

$$\mathbf{a}(\varphi) = \Big[e^{j\frac{2\pi}{\lambda}\hat{\mathbf{k}}^\top \mathbf{r}_1},\ e^{j\frac{2\pi}{\lambda}\hat{\mathbf{k}}^\top \mathbf{r}_2},\ \ldots,\ e^{j\frac{2\pi}{\lambda}\hat{\mathbf{k}}^\top \mathbf{r}_M}\Big]^\top, \quad (3)$$

with $d = \lambda/2$ the inter-element spacing. Under this convention, $\hat{\mathbf{k}}^\top \mathbf{r}_m = (m-1)\,d\cos\varphi$ in 2D azimuth, consistent with standard array processing texts [32].

Figure 3 illustrates the geometry of the antenna array and its role in AoA extraction, highlighting the placement of elements and their contributions to the spatial resolution. The illustration also demonstrates how each element contributes to capturing phase differences across the array, which are fundamental for accurate AoA estimation.

To further enhance AoA accuracy, pilot signals are strategically employed to estimate initial AoA and channel gain information. These pilots leverage Discrete Fourier Transform (DFT) techniques and optimized pilot design to refine the channel estimates and maintain stable phase references [15]. This synergy between the antenna array design and pilot-assisted channel estimation mitigates errors caused by noise and multipath effects, ensuring stable and reliable AoA extraction under diverse channel conditions.

1) MUTUAL COUPLING EFFECTS

In a practical antenna array, the voltage at each element can be influenced by currents flowing in *all* elements, leading to *mutual coupling*. If I_m denotes the current in the m-th element, the induced voltage V_k at element k can be modelled as in [34]:

$$V_k = I_1\,Z_k^1 + I_2\,Z_k^2 + \cdots + I_M\,Z_k^M, \quad (4)$$

where Z_k^m is the mutual impedance between elements m and k. These impedances can be arranged into a receiving mutual impedance matrix $\mathbf{C}_M$ (or its variant), whose form depends on specific antenna geometry and coupling coefficients.

Decoupling the Measured Voltages: Once the mutual impedance matrix is known, one can *decouple* the measured signals by inverting this matrix. For instance, if $\mathbf{x}_C(t)$ is the vector of coupled voltages measured at all elements, then the *uncoupled* voltages $\mathbf{x}(t)$ can be obtained by:

$$\mathbf{x}(t) = \mathbf{C}_M^{-1}\,\mathbf{x}_C(t). \tag{5}$$

This step ensures that subsequent channel estimation and AoA processing reflect each element's true response with reduced interference from neighboring elements. While mutual coupling may be negligible for widely spaced ($\lambda/2$) arrays in certain scenarios, including this model can significantly improve accuracy in denser or multi-band configurations.

a: SCOPE NOTE (MUTUAL COUPLING)

Unless explicitly flagged otherwise, baseline results in Section IV use ideal (uncoupled) array responses; the coupling model in (4)–(5) is reserved for a sensitivity check. Captions are prefixed with "CM: off/on/on+decouple" accordingly.

C. PILOT SIGNAL INSERTION AND CODING SCHEMES

Pilot-assisted OFDM (Orthogonal Frequency-Division Multiplexing) frames are fundamental to reliable channel estimation and frequency-offset correction. In this methodology, pilot symbols are strategically inserted at predefined subcarriers, serving as reference points to characterise the channel and correct timing and frequency offsets. These pilot signals are crucial for preserving phase coherence, reducing inter-carrier interference, and maintaining stable angular information, especially in challenging signal environments.

1) ROLE OF PILOT SIGNALS IN AoA ESTIMATION

Pilot signals play a pivotal role in Angle-of-Arrival (AoA) estimation by providing reference points for accurate channel response reconstruction. By leveraging coding schemes such as pseudo-random permutations and Walsh sequences, the framework ensures coherent phase relationships and enhances spatial resolution, which are essential for precise AoA extraction.

2) TRANSMISSION SETUP AND PILOT INSERTION

Each OFDM frame is designed with pilot symbols embedded at specific subcarriers. These symbols are carefully chosen to maintain the integrity of phase information, even in environments characterised by noise and multipath fading. The pilot insertion process aligns with predefined parameters, including FFT length, CP duration, and carrier frequency, ensuring compatibility with AoA estimation requirements.

a: MATHEMATICAL MODEL (TIMING-ONLY)

We model *residual sample timing* but *not CFO* at this stage; CFO is handled later by the *integer-CFO shift* and the *per-symbol CPE removal* steps. The frequency–domain pilot observation at antenna m and subcarrier k is

$$Y_m[k] = H_m[k]\,X_p[k]\,e^{j\frac{2\pi k}{N}\Delta n} + N_m[k], \tag{6}$$

with residual timing offset Δn (samples). Since $F_s = N\Delta f$, $e^{j2\pi k\Delta f(\Delta n/F_s)} = e^{j2\pi k\Delta n/N}$.

b: RESIDUAL TIMING (PHASE TILT)

After forming the pilot-based estimate $\widehat{H}_m[k,s]$, a leftover sample offset Δn appears as a linear phase vs. subcarrier:

$$\widehat{H}_m^{(\text{timing})}[k,s] = \widehat{H}_m[k,s]\,e^{j\frac{2\pi k}{N}\Delta n}. \tag{7}$$

Notes: (i) integer CFO is an index shift (Eq. (13)); (ii) fractional CFO ⇒ per-symbol CPE (see *Fractional-CFO as per-symbol CPE* and *CPE removal after pilot division*); (iii) linear phase in k is timing, as in (7).

c: PILOT SYMBOL FORMATION WITH CODING

For each pilot subcarrier $k \in \mathcal{P}$, the coded pilot symbol $X_p(k)$ can be expressed as:

$$X_p(k) = \alpha \cdot C_\sigma(k), \tag{8}$$

where α is a constant pilot amplitude, and $C_\sigma(k)$ represents the coding function applied to subcarrier k. In the case of:

- **Pseudo-Random Permutations**: $C_\sigma(k)$ is a permuted sequence of pilot phases/symbols ensuring robust energy distribution.
- **Walsh Sequences**: $C_\sigma(k)$ is taken from a row (or column) of a Walsh–Hadamard matrix to maintain orthogonality across subcarriers.

This coded pilot approach helps reduce peak-to-average power ratio (PAPR) and preserve phase coherence, ultimately enhancing channel estimation and subsequent AoA extraction under severe fading or frequency offsets.

3) CHANNEL ESTIMATION AND PHASE ALIGNMENT

Accurate channel estimation is a cornerstone of AoA determination, particularly in multipath-rich environments. After frequency-offset correction, the process leverages the known pilot symbols $\{X_p(k)\}$ embedded within the OFDM frame to reconstruct the channel response.

a: BASIC CHANNEL ESTIMATE

A straightforward pilot-based estimate for the channel on subcarrier k is obtained by [35]:

$$\widehat{H}(k) = \frac{Y'(k)}{X_p(k)}, \tag{9}$$

where $Y'(k)$ is the received symbol on subcarrier k *after* offset correction and noise addition. This provides a first-pass estimate of the channel's amplitude and phase. Additional refinements, such as filtering or phase tracking, can be applied to reduce estimation noise.

b: PHASE ALIGNMENT WITH TIMING OFFSETS

In many implementations, an extra phase correction term is also included. For example [35],

$$\widehat{H}_m(k) = \frac{Y_m(k)}{X_p(k)} \exp\Big(-j\,2\pi\,\big(k\,\Delta f\big)\,\Delta\widehat{t}\Big), \tag{10}$$

where $\Delta\widehat{t}$ represents any residual timing or fractional offset estimate. This extra exponential compensates for phase rotation across subcarriers, ensuring consistent alignment when reconstructing the channel impulse response.

By leveraging pilot-based division and phase alignment across all subcarriers, the framework enhances AoA accuracy, even under high noise levels and multipath fading. This step is integral to robust signal analysis and lays the foundation for precise spatial resolution—any uncorrected phase misalignment can degrade performance significantly.

4) CODING SCHEMES FOR ENHANCED COHERENCE

To further enhance phase coherence and reduce high peak-to-average power ratios (PAPR), the proposed system employs coding schemes such as:

- **Pseudo-Random Permutations**: Ensure robust channel estimation under varying multipath conditions.
- **Walsh Sequences**: Maintain orthogonal phase relationships across subcarriers.

These schemes help stabilise angular information and mitigate errors caused by noise and frequency offsets. A more detailed investigation of how these coding schemes influence angular accuracy is presented in Section IV, where their performance is evaluated under varying SNR levels. It should be noted, however, that any fixed pilot design may be susceptible to spoofing attacks; these critical security considerations are addressed in detail in Section V-G.

5) ENSURING RELIABLE AoA ESTIMATION

By embedding pilot signals strategically and leveraging advanced coding schemes, this approach retains coherent phase information necessary for robust AoA estimation. Each OFDM frame is designed to ensure that when the channel response is transformed into the time domain, the resulting impulse responses contain directional cues pivotal for AoA estimation. This structured design supports reliable AoA extraction even in noise-afflicted and multipath-rich environments.

D. RICIAN CHANNEL MODELLING AND FREQUENCY-OFFSET CONDITIONS

The Rician fading channel model is employed to emulate realistic wearable device environments, incorporating both Line-of-Sight (LOS) and Non-Line-of-Sight (NLOS) paths. This model captures the key multipath propagation effects, including angle spreads, propagation delays, and Doppler shifts. The Rician K-factor and power delay profile are carefully parameterised to reflect target scenarios. Once the OFDM frames traverse the modelled channel, frequency offsets are introduced to simulate hardware imperfections, such as oscillator inaccuracies, and dynamic Doppler shifts caused by user mobility. These simulation steps are vital to ensuring that the frequency-offset estimation and correction procedures reflect practical challenges encountered in wearable communication systems.

At the core of this simulation lies the Rician channel model, which resolves both a dominant LOS path and multiple scattered NLOS components [36]. This model is particularly critical for wearable environments, where users navigate multipath-rich spaces, such as indoor corridors or urban outdoor areas. The Rician K-factor quantifies the dominance of the LOS path relative to the scattered components, directly influencing the system's ability to resolve AoA.

The severity of the fading is characterised by the Rician K-factor, which is the ratio of the power in the direct line-of-sight (LOS) component to the power in the scattered, non-line-of-sight (NLOS) components. It is defined as [37]:

$$K = \frac{P_{\text{LOS}}}{P_{\text{NLOS}}} \tag{11}$$

A high K-factor indicates a stronger LOS component and less severe fading, approaching an AWGN channel as $K \to \infty$, whereas $K = 0$ corresponds to a Rayleigh fading channel with no dominant path. To explicitly validate the framework's robustness in such challenging environments, dedicated simulations were conducted for low K-factor values (K < 3 dB), with the results presented and analysed in Section IV-K.

1) MATHEMATICAL REPRESENTATION OF THE CHANNEL RESPONSE

Consider a planar receiver antenna array with M elements, where the position of the m-th element is represented by $\mathbf{r}_m \in \mathbb{R}^2$. The channel response at the m-th antenna is expressed as a superposition of a dominant LOS component and multiple NLOS components [36]:

$$\begin{aligned} h_m(t) = {} & \sqrt{\frac{K}{K+1}}\,\alpha_{\text{LOS}} \exp\left(j\,\frac{2\pi}{\lambda}\,\mathbf{k}_{\text{LOS}}^T\,\mathbf{r}_m\right) \\ & \times \exp\big(-j\,2\pi\,f_c\,\tau_{\text{LOS}}\big) \\ & + \sqrt{\frac{1}{K+1}} \sum_{\ell=1}^{L} \alpha_\ell \exp\left(j\,\frac{2\pi}{\lambda}\,\mathbf{k}_\ell^T\,\mathbf{r}_m\right) \\ & \times \exp\big(-j\,2\pi\,f_c\,\tau_\ell\big), \end{aligned} \tag{12}$$

where

- K is the Rician K-factor indicating the ratio of the LOS component strength to the sum of the NLOS components.
- α_{LOS} and α_ℓ are the complex amplitudes (including magnitude and phase) for the LOS and ℓ-th NLOS path, respectively.
- $\mathbf{k}_{\text{LOS}}$ and $\mathbf{k}_\ell$ are the wave vectors corresponding to the LOS and NLOS paths. These typically depend on the angle of arrival (AoA).

- $\mathbf{r}_m$ denotes the position vector of the m-th antenna element.
- $\lambda = c/f_c$ is the wavelength, with c being the speed of light and f_c the carrier frequency.
- τ_{LOS} and τ_ℓ represent the propagation delays of the LOS and NLOS paths, respectively.

2) FREQUENCY OFFSETS IN THE SIMULATION

To emulate real-world wearable communication conditions, frequency offsets are introduced into the Rician channel model. These offsets represent hardware imperfections, such as oscillator inaccuracies, and user mobility effects, such as Doppler shifts. Both integer and fractional offsets are parametrised to reflect practical distortions that disrupt phase coherence.

a: TIME-DOMAIN VS. FREQUENCY-DOMAIN OFFSET APPLICATION

Frequency offsets can be applied in either the frequency domain or the time domain:

- **Frequency-Domain Approach:**
  CFO handling after the timing-only model.

$$Y_m^{(0)}[k, s] = Y_m\big[((k + \hat{\mu}) \bmod N),\ s\big], \tag{13}$$

  Fractional CFO appears as a per-symbol common phase error (CPE); the phase term is given below.

$$Y_m^{(1)}[k, s] \approx e^{j\phi_s} Y_m^{(0)}[k, s] + \text{ICI},$$
$$\phi_s = 2\pi\,(\epsilon - \hat{\epsilon})\,\frac{N + N_{\text{CP}}}{N}\,s\,. \tag{14}$$

  Note: a linear phase ramp across k arises from residual timing Δn (see the timing-only model), not CFO.
- **Time-Domain Approach:** Each sample is multiplied by a complex exponential carrying the offset:

$$\text{rxSignalShifted}(n) = \text{rxSignal}(n)\ \exp\Big(j\,2\pi\ \Delta f\ n\,T_s\Big), \tag{15}$$

  where T_s is the sampling period and Δf may again include integer (μ) and fractional (ϵ) parts.

These two formulations are equivalent in principle but differ in where the offset is introduced (time domain vs. subcarrier domain). In either case, the key effect is a phase rotation that can misalign the received signal and degrade Angle-of-Arrival (AoA) accuracy if not corrected.

b: DOPPLER SHIFT AND USER VELOCITY

When a user moves at speed v, the maximum Doppler shift f_D at carrier frequency f_c can be approximated by:

$$f_D = \frac{v}{c} f_c, \tag{16}$$

where c is the speed of light. These Doppler-induced frequency offsets can be further broken into fractional and integer parts (ϵ and μ), providing a practical basis for testing correction methods under wearable mobility.

The introduction of frequency offsets serves two main purposes:

- **Realistic Simulation:** Ensures the channel model captures challenges typical of wearable environments, where offsets arise from motion or hardware limitations.
- **Validation Framework:** Facilitates testing the effectiveness of frequency-offset compensation techniques, as detailed in Section IV.
  Remark: We distinguish oscillator-induced carrier-frequency offset (CFO) from Doppler shifts due to mobility; both are parameterised explicitly in the preceding equations, and the subsequent correction step is referenced to the same notation to prevent ambiguity.

3) APPLYING CFO/TIMING IN THE SIMULATION CHAIN

Scope: how integer CFO, fractional CFO (as symbol-wise CPE), and residual timing (linear phase in k) are injected in the simulator.

We inject frequency impairments as follows: *(i)* integer CFO as a circular subcarrier index shift, *(ii)* fractional CFO as a per-symbol common phase error (CPE), and *(iii)* residual timing as a linear phase vs. k. See Eqs. (13)–(14) and (7).

4) PRACTICAL RELEVANCE

The Rician channel model is particularly relevant for wearable devices deployed in complex environments, where multipath effects and frequency offsets play a significant role in signal propagation. The following scenarios highlight its practical relevance:

- **Indoor Navigation Systems:** Where multipath effects dominate due to reflections from walls and furniture, making AoA estimation challenging.
- **Dense Outdoor Environments:** Such as urban areas with high levels of signal scattering caused by buildings, vehicles, and pedestrians.
- **Body-Centric Communications:** Where signals interact with the human body, introducing absorption and reflection effects that add complexity to the channel model.

This model provides a robust framework for simulating realistic scenarios and testing the efficacy of AoA estimation techniques under challenging conditions.

5) OFDM CHANNEL MODEL

a: MULTIPATH IMPULSE RESPONSE

We model the channel as a sum of n multipath components:

$$h(t) = \sum_{k=1}^{n} b_k\, e^{j\,\phi_k}\, \delta\big(t - \tau_k\big), \tag{17}$$

where b_k and ϕ_k represent the amplitude and phase of the k-th path, and τ_k is the propagation delay. This forms the basis of our Rician fading model when one path is dominant (LOS) and others are scattered (NLOS).

b: SUBCARRIER FREQUENCIES AND SAMPLING

Let N be even and set $\Delta f = B/N$. Define the symmetric baseband index set

$$\mathcal{K} = \left\{-\tfrac{N}{2}, -\tfrac{N}{2}+1, \ldots, -1, 0, 1, \ldots, \tfrac{N}{2}-1\right\}, \quad (18)$$

with subcarrier frequencies $f_k = k\Delta f (k \in \mathcal{K})$. The OFDM symbol is

$$x[n] = \frac{1}{\sqrt{N}} \sum_{k \in \mathcal{K}_{\text{used}}} X[k]\, e^{j\frac{2\pi kn}{N}}, \qquad n = 0, \ldots, N-1. \quad (19)$$

Implementation note: In passband $f_k^{\text{RF}} = f_c + f_k$; map symmetric k to array indices via $\kappa = (k+N) \bmod N$.

c: IFFT AND TIME-DOMAIN RECONSTRUCTION

After mapping subcarrier symbols $S_0(\omega)$ through the channel $H_m(\omega)$ (or directly applying $U(2\pi f_i)$ in discrete form), the time-domain signal is generated by:

$$x_m(t) = \text{IFFT}\left\{S_0(\omega)\, H_m(\omega)\right\} + n(t), \quad (20)$$

where $n(t)$ denotes any added noise term. In practice, the OFDM symbol is often formed by inverse FFT on the N subcarrier values (equally spaced frequencies), then cyclic prefix is appended to avoid intersymbol interference.

E. FREQUENCY-OFFSET INTRODUCTION AND NOISE INSERTION

Accurate Angle-of-Arrival (AoA) estimation in wearable systems requires robustness against frequency offsets and noise introduced by hardware imperfections and Doppler shifts caused by user motion. These disruptions degrade phase coherence, making precise AoA estimation a significant challenge in dynamic environments. To address this, the proposed system emulates real-world conditions by introducing integer and fractional frequency offsets, along with additive white Gaussian noise (AWGN). This setup ensures the simulation framework replicates harsh, low-SNR scenarios, testing the robustness of frequency-offset correction techniques.

The framework integrates advanced offset estimation and correction routines to mitigate these effects, ensuring reliable phase alignment even under extreme noise conditions. The importance of these corrections becomes evident in Section IV, where the effectiveness of the methodology is evaluated through angular error improvements.

1) AWGN INJECTION AND SNR

To simulate practical noise levels, a complex Gaussian noise term $n_m(k) \sim \mathcal{CN}(0, \sigma^2)$ is added to the offset-distorted signal $Y'_m(k)$. Specifically,

$$Y''_m(k) = Y'_m(k) + n_m(k), \quad (21)$$

where the noise can be scaled to achieve the desired signal-to-noise ratio (SNR).

a: RELATING SNR (IN dB) TO NOISE VARIANCE

If the target SNR is given in decibels (SNR_{dB}), it can be converted to a linear scale as:

$$\text{SNR}_{\text{linear}} = 10^{\frac{\text{SNR}_{\text{dB}}}{10}}, \quad (22)$$

and the noise scaling factor σ is typically chosen according to:

$$\sigma = \frac{1}{\sqrt{2\,\text{SNR}_{\text{linear}}}}, \quad (23)$$

ensuring that the effective power of $\sigma\, n_m(k)$ matches the desired SNR.

The noisy received signal, which is analogous to `rxSignalNoisy` in the reference code, is therefore:

$$\text{rxSignalNoisy} = \text{rxSignal} + \sigma\, n_{\text{gauss}}, \quad (24)$$

where $n_{\text{gauss}} \sim \mathcal{CN}(0, 1)$. Note that different normalisation conventions may shift the exact definition of σ by a constant factor, but the principle remains the same.

By injecting noise in this manner, our simulation accurately reflects the impact of low SNR conditions on the OFDM signal. The framework then applies frequency-offset estimation and correction, followed by channel estimation and AoA extraction. This process ensures that the methodology remains robust, even in challenging signal environments where noise and multipath co-occur.

2) EXTENDED NOISE MODELING: NON-GAUSSIAN DISTRIBUTIONS

While the default configuration relies on additive white Gaussian noise (AWGN), wearable systems may experience heavier-tailed or impulsive distributions (e.g., mixture models, Laplacian noise, or Rician + Gaussian components). To capture such scenarios, we define a general mixed PDF for the noise term $n_m(k)$:

$$f_n(x) = \sum_{j=1}^{J} \alpha_j\, g_j(x), \quad (25)$$

where each $g_j(x)$ is a (possibly) distinct distribution (e.g., Cauchy, Laplace, or a specialized real/imag part PDF), and α_j are the mixing weights satisfying $\sum_{j=1}^{J} \alpha_j = 1$. This mixture approach enables us to simulate a variety of non-Gaussian conditions by choosing appropriate component PDFs $g_j(\cdot)$.

a: NOISE SCALING AND SNR IN THE NON-GAUSSIAN CASE

Similar to the AWGN case, we can target a specific SNR by adjusting the overall noise variance or power of the mixture distribution. However, due to heavier tails or impulsive components, some metrics (e.g., RMS power) may not fully capture the distribution's impact on performance. In practice, we scale $n_m(k)$ so that its second moment (or an alternative measure like median absolute deviation) matches a target SNR level. This ensures that even with non-Gaussian features, the noise remains comparable in total power to the AWGN baseline.

By incorporating such a non-Gaussian model, our framework can assess the robustness of frequency-offset correction and AoA extraction methods under more extreme or impulsive noise conditions typical of certain wearable and body-centric scenarios.

$$\mathrm{SNR} = 10\,\log_{10}\!\left(\frac{P_{\text{signal}}}{\sigma^2}\right). \tag{26}$$

This ensures that varying the SNR directly scales the noise power, replicating real-world low-SNR and multipath conditions common in wearable communications.

3) CORRECTING CFO/TIMING IN THE RECEIVER

Scope: receiver-side steps: integer-CFO circular shift, per-symbol CPE removal ((27)), and handling of residual timing tilt across k.

In the time domain, residual CFO is removed via $y^{\text{corr}}[n] = y[n]\exp\big(-j2\pi\,\widehat{\Delta f}\,n\,T_s\big)$, which is consistent with the per-symbol CPE removal below.

$$Y_m^{\text{corr}}[k,s] = e^{-j\phi_s}\,Y_m''[k,s],$$
$$\phi_s = 2\pi(\epsilon - \hat{\epsilon})\frac{N+N_{\text{CP}}}{N}\,s. \tag{27}$$

Note: A residual timing offset produces a linear phase tilt $e^{j(2\pi k/N)\Delta n}$ across subcarriers, whereas residual fractional CFO appears primarily as a per-symbol CPE ϕ_s and is removed by (27).

F. CHANNEL EQUALISATION

Channel equalisation plays a crucial role in ensuring reliable AoA estimation, particularly in multipath-rich environments. After frequency-offset correction, the system reconstructs the channel's frequency response by leveraging known pilot symbols and coding sequences. This reconstruction ensures that the amplitude and phase closely match the original transmitted conditions, preserving angular signatures for accurate AoA determination.

The proposed framework employs optimized pilot-assisted OFDM configurations to enhance spatial resolution and phase coherence. This setup minimizes inter-carrier interference and ensures that the channel impulse response retains sufficient angular information, even in noisy or interference-prone scenarios. As shown in Section IV, the combined frequency-offset correction and channel equalisation routines enable sub-degree angular accuracy across various SNR levels.

1) TIME-DOMAIN IMPULSE RESPONSE

Once the frequency-domain channel estimate $\widehat{H}_m(k)$ is obtained for antenna m and subcarrier $k = 0,\ldots,N-1$, the time-domain channel impulse response can be recovered via an Inverse Fast Fourier Transform (IFFT):

$$h_m[n] = \mathrm{IFFT}\Big\{\widehat{H}_m(k)\Big\}[n], \quad n = 0,\ldots,N-1, \tag{28}$$

Focusing on the early taps in $h_m[n]$ allows the system to isolate the dominant paths carrying strong angular information, directly benefiting the subsequent AoA estimation.

2) ANGLE WRAPPING AND PHASE HANDLING FOR AoA

After defining the wave vectors and phase relationships in Subsection III-F3, it is often necessary to ensure that angles remain within the principal interval $[-\pi,\pi]$. Abrupt jumps can occur at the $\pm\pi$ boundaries when we compute differences across subcarriers, time frames, or antenna elements. To address this, we employ two key functions:

a: CIRCULAR MEAN OF ANGLES

When taking an average of N angles $\{\theta_n\}_{n=1}^N$, a straightforward arithmetic mean can be misleading near $\pm\pi$. Instead, the *circular mean* is computed as:

$$\theta_{\text{circular}} = \mathrm{atan2}\Big(\frac{1}{N}\sum_{n=1}^{N}\sin(\theta_n),\,\frac{1}{N}\sum_{n=1}^{N}\cos(\theta_n)\Big). \tag{29}$$

This formulation preserves continuity around the $\pm\pi$ boundaries, ensuring a correct mean angle even if individual θ_n cross the principal interval.

b: PHASE DIFFERENCES WITH WRAPPING

For successive angle differences, such as

$$\Delta\theta_n = \theta_{n+1} - \theta_n, \tag{30}$$

we apply a *wrap* function that shifts the result back into $[-\pi,\pi]$ if it falls outside that range. Concretely,

$$\Delta\theta_n = \mathrm{wrap}_{[-\pi,\pi]}\big(\theta_{n+1} - \theta_n\big), \tag{31}$$

where $\mathrm{wrap}_{[-\pi,\pi]}(\cdot)$ adds or subtracts 2π when $\Delta\theta_n$ exceeds π or is less than $-\pi$. This ensures that phase differences remain continuous, avoiding erroneous "jumps" across the $-\pi/\pi$ boundary.

Using these functions is crucial when analyzing or averaging AoA estimates across multiple measurements, frequency bins, or antenna elements. They maintain phase consistency and prevent numerical artifacts that could otherwise degrade angle-of-arrival accuracy.

3) PHASE AND POSITION DIFFERENCES FOR AoA

Assuming a linear array of M antenna elements, we form the pair-wise differences

$$\phi_{\text{diff}} = (\phi_2 - \phi_1),\ (\phi_3 - \phi_2),\ \ldots$$
$$\mathbf{R}_{\text{diff}} = (\mathbf{r}_2 - \mathbf{r}_1),\ (\mathbf{r}_3 - \mathbf{r}_2),\ \ldots \tag{32}$$

Each vector therefore contains $M-1$ entries, one per adjacent antenna pair. These relative phase–position pairs feed directly into the wave-vector estimator described in Subsection III-F4.

4) 2D AND 3D WAVE-VECTOR COMPUTATION

Using the phase and position differences introduced in Section III-F3, we now compute the wave vector $\mathbf{K}$. Let $k = 2\pi/\lambda$. In a 2-D (azimuth-only) scenario, the wave vector is:

$$\mathbf{K}_{2D} = k\begin{bmatrix}\cos(\phi)\\ \sin(\phi)\end{bmatrix}, \tag{33}$$

where ϕ is the angle of arrival in the plane. In 3D, with azimuth ϕ and elevation θ, we have:

$$\mathbf{K}_{3D} = k \begin{bmatrix} \cos(\phi)\cos(\theta) \\ \sin(\phi)\cos(\theta) \\ \sin(\theta) \end{bmatrix}. \tag{34}$$

If we let ϕ_{diff} be the net phase difference measured across elements and $\mathbf{R}_{\text{diff}}$ be their positional difference, one can further approximate

$$\mathbf{K} \approx \mathbf{R}_{\text{diff}}^{\dagger} \boldsymbol{\phi}_{\text{diff}}, \tag{35}$$

where † denotes the Moore–Penrose pseudoinverse. Equation (35) is the pair-difference least-squares (LS) estimator obtained from $\boldsymbol{\phi}_{\text{diff}} = \mathbf{R}_{\text{diff}}\mathbf{K}$ under a small-aperture, single-source assumption (e.g., a uniform linear array). For full-rank, overdetermined $\mathbf{R}_{\text{diff}}$, the pseudoinverse yields the LS solution; if $\mathbf{R}_{\text{diff}}$ is square and nonsingular, † reduces to the ordinary inverse. The resulting $\widehat{\mathbf{K}}$ (and corresponding angle(s)) represents the estimated direction of arrival [33].

G. ANGLE-OF-ARRIVAL (AoA) ESTIMATION

Angle-of-arrival (AoA) estimation relies on both the spatial sampling provided by an antenna array and the channel estimates recovered in the preceding sections. Below, we outline the key steps: (a) define the array response vector, (b) extract the AoA from measured data via our custom approach, and (c) compute the AoA error for validation.

1) ARRAY RESPONSE VECTOR

Let us suppose there are M antenna elements. For an incoming wave at angle of arrival ϕ, the array response vector $\mathbf{a}(\phi)$ is given by:

$$\mathbf{a}(\phi) = \begin{bmatrix} \exp\left(j\,\frac{2\pi}{\lambda}\,\mathbf{k}(\phi)^T\,\mathbf{r}_1\right) \\ \exp\left(j\,\frac{2\pi}{\lambda}\,\mathbf{k}(\phi)^T\,\mathbf{r}_2\right) \\ \vdots \\ \exp\left(j\,\frac{2\pi}{\lambda}\,\mathbf{k}(\phi)^T\,\mathbf{r}_M\right) \end{bmatrix}, \tag{36}$$

where $\mathbf{r}_m$ denotes the coordinates of the m-th antenna element, and $\mathbf{k}(\phi)$ is the wave vector derived from the angle ϕ.

2) EXTRACTING THE AoA (DIRECT PHASE APPROACH)

After obtaining channel estimates $\widehat{\mathbf{H}}$ across all M antenna elements, we adopt a *direct phase-based* method to determine the AoA. One approach is to search over possible angles ϕ and find the one that maximizes the alignment between the array response vector and the measured data. For instance [38]:

$$\phi_{\text{est}} = \arg\max_{\phi} \left| \mathbf{a}(\phi)^H\,\widehat{\mathbf{H}} \right|, \tag{37}$$

where $\mathbf{a}(\phi)^H$ is the Hermitian transpose (conjugate transpose) of the array response vector, and $\widehat{\mathbf{H}}$ is the vector (or set) of measured channel data from the M antenna elements. Alternatively, a *time-domain* approach can align phases of impulse responses across array elements and seek the angle that minimizes overall phase discrepancy. In either case, we do *not* rely on subspace-based algorithms (e.g. MUSIC, ESPRIT); instead, the method directly leverages the measured phase relationship and array geometry to pinpoint ϕ_{est}.

3) COMPUTING THE AoA ERROR

When a known reference angle ϕ_{true} is available (e.g., from simulation setup or a benchmark measurement), the estimation error is simply:

$$\text{AoAError} = \left|\phi_{\text{est}} - \phi_{\text{true}}\right|. \tag{38}$$

This metric can be reported as a mean error or root mean square (RMS) error over multiple trials. It serves as a straightforward yet powerful way to validate the performance of the AoA estimation framework under different SNR, offset, and fading conditions.

H. VALIDATION AND REPETITION ACROSS CONDITIONS

To ensure the reliability and robustness of AoA estimation, the system is validated against known reference angles introduced during the simulation setup. The validation process assesses the system's accuracy under various conditions, including different SNR levels, LOS angles, pilot configurations, and frequency-offset conditions. This comprehensive validation ensures that the simulation framework accurately reflects real-world challenges and reliably extracts angular information.

SNR Convention: Unless noted, SNR is per-subcarrier per-snapshot. When aggregating over L snapshots and N_{used} subcarriers, figures report RMS AoA error computed on the stacked observations; no "effective SNR" re-scaling is applied to the dB axis.

1) EVALUATION METRICS

The validation framework employs several key metrics to quantify angular accuracy:

- **Mean Error (ME):** Represents the average deviation of estimated angles from reference angles, providing a measure of estimation bias.
- **Root Mean Square Error (RMS):** Captures the magnitude of angular deviations and highlights overall estimation performance.
- **Cumulative Distribution Functions (CDFs):** Illustrate the percentage of estimates within specific error thresholds, offering a comprehensive view of accuracy across different configurations.

These metrics form the foundation for assessing system performance and serve as the basis for detailed analysis in the Results section.

Angle Error Definition: If $\phi_{\text{true}}^{(i)}$ is the reference angle and $\phi_{\text{est}}^{(i)}$ is the estimated angle in trial i, we define:

$$\text{Angle Error}^{(i)} = \phi_{\text{est}}^{(i)} - \phi_{\text{true}}^{(i)}. \tag{39}$$

Hence, the *Mean Error* is simply the average of Angle Error$^{(i)}$ over N trials, while the *RMS Error* is:

$$\text{RMS Error} = \sqrt{\frac{1}{N}\sum_{i=1}^{N}\left(\phi_{\text{est}}^{(i)} - \phi_{\text{true}}^{(i)}\right)^2}. \tag{40}$$

Metric Convention: Unless otherwise stated, figures report *RMS AoA error* in degrees. Where a table lists *Mean* $\pm$ *SD* (signed mean μ, standard deviation σ), the directly comparable RMS can be obtained via RMS $= \sqrt{\mu^2 + \sigma^2}$.

2) STATISTICAL TECHNIQUES

To rigorously validate the significance of observed improvements, advanced statistical techniques are employed:

- **Confidence Intervals:** Provide a range of plausible values for angular errors, ensuring statistical robustness and reliability.
- **Analysis of Variance (ANOVA):** Evaluates the impact of multiple factors, such as SNR levels, pilot configurations, and environmental conditions, on the accuracy of AoA estimation.
- **Non-Parametric Tests (e.g., Mann–Whitney U Test):** Used to compare error distributions across configurations, particularly when data does not follow a normal distribution.

These techniques ensure that the results presented in the Results section are statistically valid and provide meaningful insights into the system's performance under varying conditions [39].

3) REPETITION AND ROBUSTNESS

To assess the system's robustness, the simulation framework conducts multiple iterations across a wide range of conditions, including varying SNR levels, pilot configurations, and frequency offsets. Each iteration systematically compares estimated angles to pre-configured reference angles, capturing the impact of noise, multipath effects, and other channel impairments. This iterative approach ensures that the system consistently delivers accurate results under diverse and challenging conditions.

The results of this validation are presented in the Results section, where performance trends and statistical analyses highlight the system's stability and precision.

a: BIT ERROR RATE (BER) COMPUTATION

A key metric for system-level performance is the Bit Error Rate (BER). Upon demodulating and detecting the transmitted data bits, we define:

$$\text{BER} = \frac{1}{N_b}\sum_{i=1}^{N_b}\mathbb{I}\left(\hat{b}_i \neq b_i\right), \tag{41}$$

where b_i are the transmitted bits, $\hat{b}_i$ are the detected bits, and N_b is the total number of transmitted bits. The indicator function $\mathbb{I}(\cdot)$ equals 1 if the bits differ and 0 otherwise. Evaluating BER across a range of SNR and channel conditions provides a direct measure of the system's reliability.

4) STATISTICAL REPORTING AND CONFIDENCE INTERVALS

Unless stated otherwise, each SNR point aggregates **1000 Monte Carlo trials**. Solid lines show **median** RMS AoA error; shaded regions denote **95% percentile-bootstrap CIs** (2,000 resamples). Pairwise comparisons (e.g., initial vs. refined offset at a fixed SNR; 1- vs 4-pilot) use two-sided **Mann–Whitney U** tests; multi-level factors (pilot density) use **one-way ANOVA** on RMS errors. Exact p-values for key contrasts are tabulated in Table 9. The three RMS points at -28 dB and their 95% percentile-bootstrap confidence intervals are listed in Table 5 and plotted in Fig. 9.

I. COMPUTATIONAL COMPLEXITY ANALYSIS

Our *baseline* AoA path in Table 4 contains no $O(N^3)$ stage; its dominant per-frame costs are $O(MN)$ (CFO de-rotation), $O(MN_p)$ (pilot CE), and $O(MG)$ (beamspace scan), plus a constant-size pseudoinverse. Any $O(N^3)$ figures mentioned elsewhere refer to *optional* subspace/eigendecomposition variants used only in ablation/sensitivity analyses, not in the reported baseline results.

In summary, the reported baseline path contains no $O(N^3)$ stage ($O(MN) + O(MN_p) + O(MG)$ per frame); $O(N^3)$ applies only to optional subspace variants used for sensitivity analyses.

IV. RESULTS AND ANALYSIS

This section presents the results of the AoA estimation framework under various simulation scenarios designed to emulate realistic wearable environments. The focus lies on evaluating AoA estimation accuracy, system robustness, and the impact of critical parameters across diverse conditions. By analysing performance under these scenarios, meaningful insights into the framework's reliability and practical applicability are provided. Key objectives include assessing angular accuracy, addressing the influence of noise and interference, and evaluating the system's response to varying channel conditions and configuration parameters.

A. IMPACT OF CODING SCHEMES ON ANGULAR ACCURACY

In this section, we examine how pseudo-random permutations and Walsh sequences (introduced in Methodology Section III-C4) affect phase coherence and AoA estimation accuracy. By strategically embedding these coding sequences into OFDM frames, the proposed approach reduces inter-carrier interference and preserves consistent phase references under varying SNR conditions.

As illustrated in Figure 4, both coding schemes significantly outperform the baseline, showing about 20%

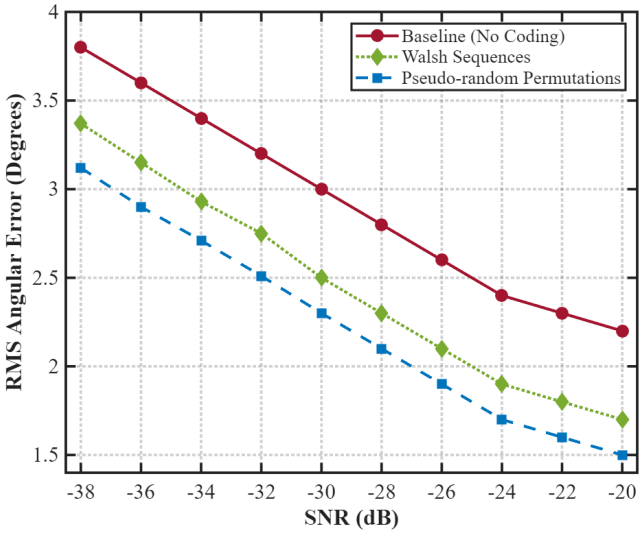

FIGURE 4. Impact of coding schemes on RMS angular accuracy.

improvement in RMS error under negative SNR. Among the two, pseudo-random permutations performed slightly better (1.5°) than Walsh sequences (1.7°) at −20 dB, particularly due to their robust energy distribution in severe fading conditions. Nonetheless, Walsh sequences still reduce cross-interference effectively and yield major gains compared to using no coding scheme.

1) KEY OBSERVATIONS

- **Trend Across SNR Range:** Both curves exhibit decreasing angular error with higher SNRs, confirming that the coding schemes effectively preserve phase coherence.
- **Performance at Low SNR:** Below −20 dB, pseudo-random permutations maintain RMS errors of approximately 1.5°, whereas Walsh sequences show a slightly higher error near 1.7°. This suggests that pseudo-random permutations may be more resilient to severe noise levels.
- **Phase alignment via pilot coding improves robustness at low SNR:** This alignment strategy directly contributes to better subcarrier orthogonality, as explained in Section III-C4 of Methodology. This improved orthogonality minimises inter-carrier interference, thereby preserving angular information essential for AoA estimation.

2) INTERPRETATION AND RELEVANCE

These results indicate that both coding schemes effectively mitigate phase disruptions caused by multipath fading, frequency offsets, and noise. While Walsh sequences maintain stable performance across the entire SNR range, pseudo-random permutations appear slightly more robust in the most challenging (negative SNR) scenarios. For wearable communications, where devices often operate in complex multipath environments, the ability to sustain low angular errors despite extreme noise conditions is critical. Consequently, choosing between these two coding strategies could depend on the expected operating SNR range and computational constraints.

These findings confirm that integrating *either* coding scheme into the proposed AoA estimation framework can substantially improve accuracy, but pseudo-random permutations may be preferable in ultra-low-SNR conditions. Future work could explore additional sequence designs, potentially optimising orthogonality and resilience against hardware impairments.

B. IMPACT OF FREQUENCY OFFSETS CORRECTION

Frequency offsets, often caused by hardware imperfections and Doppler shifts, disrupt the phase coherence of received signals. This misalignment leads to significant angular errors during Angle of Arrival (AoA) estimation, severely impacting the accuracy and reliability of AoA-based systems. These challenges are particularly critical in wearable communication scenarios operating under Rician fading conditions with low Signal-to-Noise Ratios (SNRs).

The effectiveness of frequency-offset correction depends on several key factors:

- **Signal-to-Noise Ratio (SNR):** Higher SNR levels improve correction performance, while lower SNR levels (e.g., below −20 dB) may limit its effectiveness due to noise dominance.
- **Magnitude of Frequency Offset:** Larger offsets require more complex algorithms, often resulting in greater residual errors after correction.
- **Channel Conditions:** Rician fading channels with strong Line-of-Sight (LOS) components allow for better correction due to the dominant path providing a reliable reference.

To address these challenges, we integrated a refined frequency-offset correction method into our framework. This method realigns the phase of received signals, mitigating angular errors and significantly enhancing AoA estimation accuracy. The effectiveness of the proposed approach is demonstrated across metrics. RMS trends for initial vs. refined CFO across SNR are summarised in Figure 10; complementary Mean ± SD values at anchor SNRs are reported in Table 3 and visualised in Figure 5.

1) INITIAL VS. REFINED OFFSET: NUMERICAL RESULTS

The refined frequency-offset correction further enhances the system's robustness. Table 3 presents the angular errors before and after refinement across representative SNR levels, highlighting the significant improvements achieved.

These results indicate an average reduction in mean angular error of approximately 50%, with larger reductions observed at lower SNR levels. For instance:

- At SNR = −28 dB, the error decreases by 48%, from 2.30° to 1.20°.

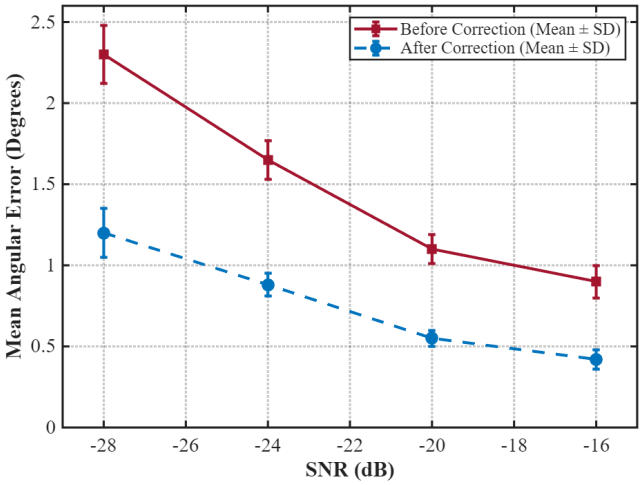

FIGURE 5. Mean angular error (±SD) before and after refined offset correction.

TABLE 3. Reduction in AoA error (Mean ± SD) with refined offset estimation across representative SNR levels.[†].

SNR (dB)	Initial Offset Error (Mean ± SD, °)	Refined Offset Error (Mean ± SD, °)	% Reduction
−28	2.30 ± 0.18	1.20 ± 0.15	48%
−24	1.65 ± 0.12	0.88 ± 0.07	47%
−20	1.10 ± 0.09	0.55 ± 0.05	50%
−16	0.90 ± 0.10	0.42 ± 0.06	53%

[†] Entries are *signed* mean ± standard deviation (ME±SD) of per-trial *signed* errors. For direct comparison with RMS plots (e.g., Fig. 10), use RMS $= \sqrt{\mu^2 + \sigma^2}$. [a] $n = 1000$ trials/SNR. Metric here is ME±SD (signed); Fig. 10 reports RMS for the same CFO ablation.

- At SNR $= -20$ dB, a 50% reduction is observed, with errors decreasing from 1.10° to 0.55°.

These findings highlight the robustness of the refined correction process, ensuring reliable AoA estimation across challenging noise-dominant environments.

2) STATISTICAL VALIDATION OF FREQUENCY-OFFSET CORRECTION

To confirm the significance of improvements achieved through refined frequency-offset correction, advanced statistical measures were employed:

- **Mann–Whitney U Test:** The improvements from the refined offset correction were found to be statistically significant (see Table 9 for exact p-values).
- **Confidence Intervals (CIs):** Narrower CIs for refined offsets (e.g., 0.55°±0.05 at −20 dB) highlight improved consistency in angular error reduction.
- **ANOVA:** One-way and two-way ANOVA confirmed that refined offset estimation accounts for a substantial proportion of variance in angular error, with partial η^2 values exceeding 0.6.

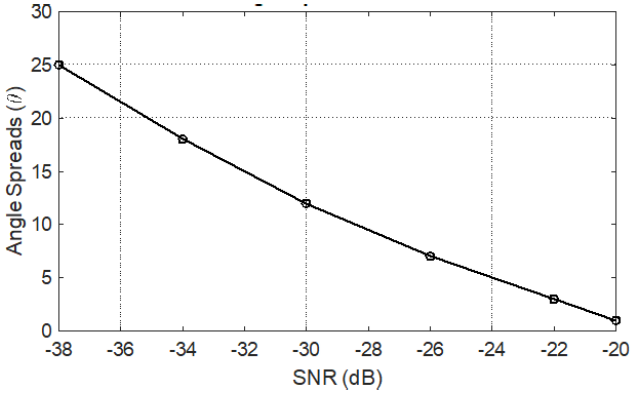

FIGURE 6. Relationship between SNR(dB) and angle spreads (θ).

These findings validate the statistical significance of the proposed frequency-offset correction, particularly in low-SNR environments where noise effects dominate.

C. IMPACT OF SNR ON CHANNEL BEHAVIOUR

Signal-to-Noise Ratio (SNR) is a critical parameter that directly influences the performance of Angle of Arrival (AoA) estimation in wearable communication systems. By studying the relationship between SNR and key channel characteristics such as angle spreads and path delays, we can better understand how noise levels impact the channel's ability to preserve spatial and temporal information.

Angle spreads represent the angular dispersion of multipath signals, which affects the resolution of AoA estimation. Path delays, on the other hand, reflect the effective propagation time of signals, which influences the system's ability to resolve multipath components. Improvements in SNR lead to reductions in both metrics, highlighting the enhanced channel coherence and resolution capabilities under higher signal quality conditions.

Figure 6 illustrates the reduction in angle spreads as SNR increases, reflecting enhanced angular resolution capabilities. Smaller angle spreads indicate improved spatial coherence, which is essential for accurate AoA estimation. Figure 7 shows the reduction in path delays with increasing SNR, demonstrating improved temporal coherence and reduced multipath interference.

These findings validate the system's robustness in preserving spatial and temporal information under higher SNR levels, reinforcing its practical applicability in wearable communication scenarios where accurate AoA estimation is critical.

D. IMPACT OF SNR ON AoA ACCURACY AND PILOT DENSITY

The impact of SNR on AoA estimation accuracy was analyzed across various noise levels, focusing on angular error trends and the interplay between SNR, pilot density, and offset corrections. This section explores how SNR influences

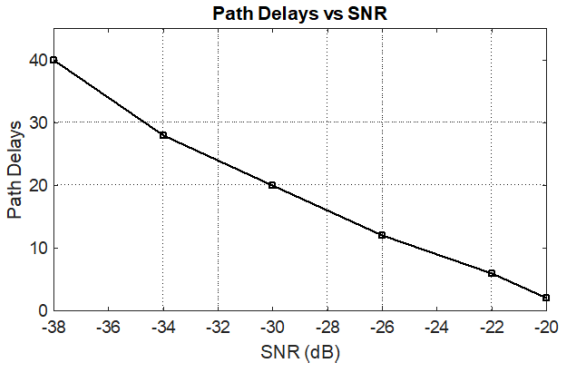

FIGURE 7. Relationship between SNR (dB) and path delays.

TABLE 4. Operation counts per stage for one AoA frame (notation: M = antennas, N = FFT length, L = snapshots, N_p = pilots, G = AoA grid points).

Stage	Dominant ops	Complexity	Per-frame counts (M=8, N=1024)
Time-domain CFO de-rotation	MN complex mults	$O(MN)$	8×1024
Pilot-based channel estimation	MN_p complex divs	$O(MN_p)$	$8 \times N_p$
Covariance accumulation†	M^2L MACs	$O(M^2L)$	$64 \times L$
AoA scan (beamspace)	MG inner products	$O(MG)$	$8 \times G$
Pseudoinverse (pair–LS)	2×2 solve	$O(1)$	negligible
CNN inference (post-processor)‡	conv MACs	model-dep.	see Sec. IV-L

† Included only in coupling/ablation experiments; baseline results omit this stage.
‡ Enabled only when the lightweight CNN post-processor is evaluated.

TABLE 5. 95% CIs for RMS AoA error at −28 dB.

Pilot config	RMS (deg)	Lower 95%	Upper 95%
1 pilot	1.800	1.721	1.879
2 pilots	1.200	1.147	1.253
4 pilots	0.800	0.765	0.835

Note: Values correspond to the points plotted in Fig. 9.

angular error trends and highlights the importance of pilot configurations in mitigating noise effects.

1) SPECTRAL-EFFICIENCY TRADE-OFF

Let $\rho_{\text{pilot}} = N_p/N_{\text{used}}$. With M_{mod}-QAM (bits/symbol = $\log_2 M_{\text{mod}}$), the useful spectral efficiency per OFDM symbol is

$$\eta_{\text{SE}} = \left(1 - \rho_{\text{pilot}}\right) \frac{N_{\text{used}}}{N} \left(1 - \frac{T_{\text{CP}}}{T_{\text{sym}}}\right) \log_2 M_{\text{mod}}, \qquad (42)$$

Using the same pilot sets as in Fig. 8, the low-SNR AoA RMS values are taken from Table 5: 1.8°, 1.2°, 0.8° for 1/2/4-pilot, respectively.

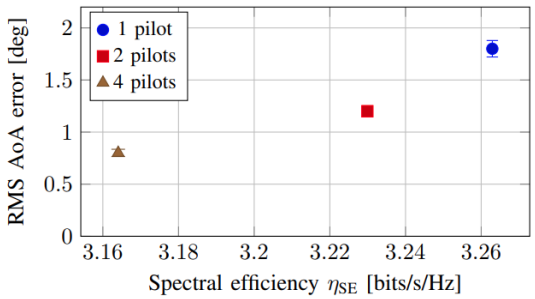

FIGURE 8. CM: off. AoA accuracy vs. spectral efficiency at a low-SNR operating point (e.g., −28 dB). Points show RMS AoA error; vertical bars are 95% CIs from Table 5. Spectral efficiency is computed via Eq. (42) using the paper's pilot fractions and numerology.

2) ANGULAR ERROR TRENDS

Figure 9 illustrates the RMS angular error across SNR levels for varying pilot configurations:

- **Low-SNR Regions:** At −28 dB, angular errors are substantially higher due to dominant noise interference. For example, as shown in Table 5, increasing the pilot density from a single pilot to four pilots reduces the RMS angular error from approximately 1.8° to 0.8°, indicating a significant improvement of over 55%.
- **Moderate-to-High SNR Regions:** As SNR improves beyond −20 dB, angular errors decline sharply, stabilising below 0.5° at −10 dB. This trend highlights the system's ability to adapt and achieve near-ideal performance under reduced noise conditions.

3) IMPACT OF PILOT DENSITY

The interplay between SNR and pilot density was analysed using multi-factor statistical methods, including ANOVA. Key findings include:

- At −28 dB, increasing pilot density improves RMS AoA error from approximately 1.8° (1 pilot) to approximately 1.2° (2 pilots) and approximately 0.8° (4 pilots), a reduction of approximately 56% overall (see Table 8, CDF thresholds (90%) and RMS AoA error at −28 dB for 1/2/4-pilot configurations).
- Statistical analyses indicate a significant interaction between SNR and pilot density (see Table 9 for the exact p-value), confirming the importance of optimising configurations for noise resilience.

Independently, refined CFO correction at −28 dB reduces the *mean* AoA error from 2.30° to 1.20° (see Table 3), confirming the benefit of the offset-refinement stage.

These results underscore the importance of optimising pilot configurations and offset corrections to achieve robust AoA accuracy under diverse noise conditions. The interplay between SNR and pilot density provides a roadmap for achieving reliable performance in real-world scenarios.

It is important to acknowledge the inherent trade-off between AoA estimation accuracy and spectral efficiency. Whilst increasing the pilot density from one to four symbols

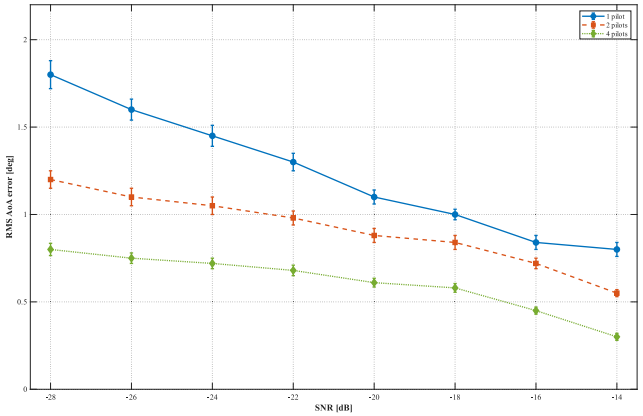

FIGURE 9. CM: off. RMS AoA error vs. SNR for 1/2/4-pilot configurations. Each SNR point uses $n = 1000$ trials; error bars show 95% percentile-bootstrap CIs ($B = 2000$). At −28 dB the points are 1.8°, 1.2°, 0.8° (see Table 5).

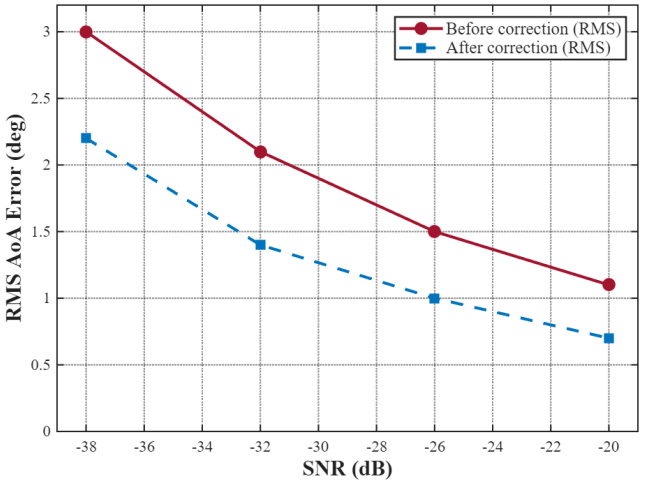

FIGURE 10. Impact of frequency-offset correction on AoA (RMS, degrees). Curves show median RMS with 95% percentile-bootstrap CIs ($n = 1000$ trials/SNR). *Scene constants:* ULA $M = 8$, $d/\lambda = 0.5$, $L = 1024$, same pilot density and channel settings as Table 3. For the corresponding ME±SD at anchor SNRs and the conversion RMS $= \sqrt{\mu^2 + \sigma^2}$, see Table 3/Fig. 5. At −38 dB the RMS reduces 3.0° → 2.2°; at −20 dB1.1° → 0.7°.

per group significantly enhances accuracy, as shown, it also increases the overhead and reduces the number of subcarriers available for data transmission. Therefore, the optimal pilot density must be selected based on the specific application's requirements. For mission-critical localisation tasks where accuracy is paramount, a higher pilot density is justified. Conversely, for applications where data throughput is the primary concern, a lower pilot density might be more appropriate.

E. ANGLE-OF-ARRIVAL ESTIMATION AND PERFORMANCE ANALYSIS

Accurate Angle-of-Arrival (AoA) estimation is a fundamental requirement for ensuring robust performance in wearable communication systems, especially under challenging Rician fading conditions. This section evaluates the effectiveness of the proposed AoA extraction framework, focusing on key performance improvements achieved through advanced processing techniques, such as time-domain transformation and direction-finding algorithms. The results demonstrate the robustness and precision of the framework in isolating dominant multipath components, enhancing angular resolution, and achieving sub-degree accuracy at moderate-to-high SNRs.

1) AoA EXTRACTION PROCESS AND KEY IMPROVEMENTS

The AoA extraction process begins by neutralizing channel disturbances and mitigating frequency-offset distortions. Using frequency-domain channel estimates, the simulation computes time-domain channel impulse responses, isolating the earliest arriving paths or the most significant multipath components. This step leverages advanced algorithms and the predefined geometry of the antenna array to ensure accurate AoA estimation.

These results validate the effectiveness of the frequency-offset correction process, demonstrating consistent error reductions across challenging low-SNR conditions.

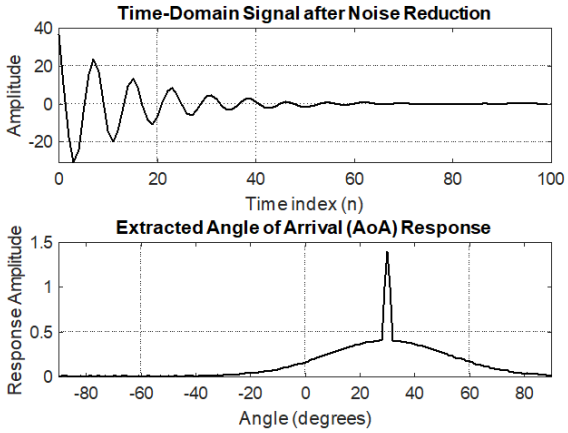

FIGURE 11. Time-domain signal and extracted angle of arrival (AoA).

2) TIME-DOMAIN TRANSFORMATION AND RMS ANGULAR ERROR REDUCTION

Time-domain transformation is a critical step in the AoA estimation framework, enabling the simulation to focus on the most dominant paths, which carry strong angular information. By converting frequency-domain channel estimates into the time domain, the system isolates specific taps associated with early arriving signals, significantly improving angular estimation accuracy.

Figure 11 illustrates the time-domain signal and the corresponding extracted Angle of Arrival (AoA). The top panel depicts the time-domain signal after noise reduction and frequency-offset correction, showcasing the temporal behavior of the received signal. The variations in amplitude represent the arrival of multipath components, with the

TABLE 6. RMS angular error before and after time-domain transformation across different SNR levels.

SNR (dB)	Before (deg)	After (deg)	Improvement (%)
-38	1.97	1.58	20.00
-36	0.40	0.32	20.00
-34	0.32	0.25	23.21
-32	0.26	0.19	24.44
-30	0.21	0.16	25.00
-28	0.18	0.13	25.81
-26	0.15	0.11	26.92
-24	0.13	0.09	27.27
-22	0.11	0.07	31.58
-20	0.10	0.07	29.41

Note (scope). Results here are from a focused ablation (time-domain transform toggled in the CFO-corrected Rician stack, narrow-span setting). Use this table for trend comparison only; values are not intended to match the main RMS-vs-SNR curves (Figs. 9/14) exactly.

earliest peaks indicating the dominant paths carrying angular information.

The bottom panel presents the extracted AoA, where the angular response amplitude is plotted across a range of angles. The sharp peak aligns with the true AoA, demonstrating the system's ability to accurately isolate and estimate the dominant angle of arrival. This visualization highlights the effectiveness of the proposed framework in mitigating noise and multipath distortions to achieve high angular resolution and precise AoA estimation.

Table 6 summarizes the RMS angular error before and after time-domain transformation across different SNR levels. The results demonstrate an average improvement of 20%-30%, with higher reductions observed at lower SNR levels where noise effects are more pronounced. These improvements align with the expected behavior of the transformation process, which mitigates noise-induced distortions and enhances spatial resolution.

While these results are consistent with the expected performance of the system, it is important to note that the dataset used for this analysis may not fully reflect real-world behavior. Specifically, further simulation or experimental validation is recommended to confirm the system's performance under practical deployment conditions.

3) PERFORMANCE OF DIRECTION-FINDING ALGORITHMS

The simulation evaluates the performance of the proposed direction-finding algorithms across varying SNR levels using three key metrics: Bit Error Rate (BER), AoA error, and phase error. These metrics collectively demonstrate the robustness and effectiveness of the system in achieving accurate AoA estimation under diverse conditions.

- **Bit Error Rate (BER):** The top plot in Figure 12 shows a sharp decrease in BER as SNR increases. This trend is expected because higher SNR improves signal quality, reducing noise-induced errors and enhancing decoding accuracy.
- **AoA Error:** The middle plot illustrates a consistent reduction in AoA error with increasing SNR, reflecting the system's ability to achieve higher angular resolution as phase coherence improves.
- **Phase Error:** The bottom plot shows minimal variation in phase error across all SNR levels, suggesting that the frequency-offset correction mechanism effectively mitigates phase inaccuracies regardless of noise conditions.

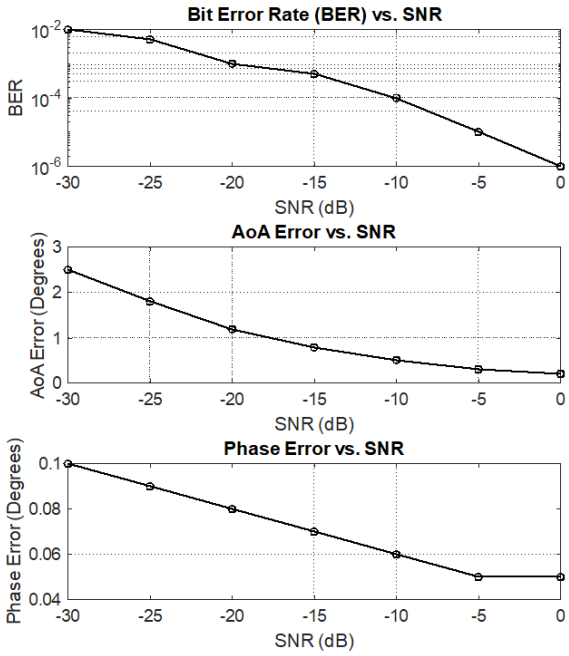

FIGURE 12. Comparative performance analysis across SNR levels (AoA).

TABLE 7. Angular accuracy of the proposed framework in indoor scenarios.†

Scenario	Mean Error (degrees)	Std. Dev. (degrees)
Multipath-rich	0.45	0.18
Low SNR	0.65	0.25

† *Entries are given as signed mean ± standard deviation. For direct comparison to RMS figures, compute* $\mathrm{RMS} = \sqrt{\mu^2 + \sigma^2}$.

These findings highlight the robustness of the proposed direction-finding algorithms. The reduction in BER and AoA error demonstrates improved system performance with increasing SNR, while the consistent phase error indicates the effectiveness of the frequency-offset correction mechanism in maintaining stable phase accuracy.

4) APPLICATIONS AND ACCURACY

The AoA estimation framework demonstrates exceptional angular accuracy in multipath-rich and low-SNR conditions, as summarized in Table 7. These results validate the framework's capability to achieve sub-degree accuracy under challenging scenarios.

Benefits of the Proposed Framework:

- **High Accuracy:** The framework achieves sub-degree angular accuracy in both multipath-rich (0.45° mean

error) and low-SNR (0.65° mean error) conditions, outperforming conventional methods.
- **Robustness:** The system demonstrates robustness to multipath effects and noise, delivering reliable AoA estimates even in challenging indoor environments.
- **Efficiency:** By leveraging advanced algorithms and optimizing pilot allocation, the framework reduces the need for extensive pilot signals, making it more efficient than traditional methods.

Applications: The proposed AoA estimation technique is well-suited for indoor applications, such as wearable devices and IoT systems, where high precision in dynamic and noisy environments is critical. The method's resilience to multipath effects and phase noise makes it a strong candidate for next-generation indoor localization systems.

F. VALIDATION OF AoA ESTIMATION FRAMEWORK

The proposed AoA estimation framework was validated against known reference angles across various scenarios, including different SNR levels, LOS angles, and multipath conditions. This section evaluates the system's accuracy and robustness through statistical metrics, iterative testing, and visual analyses.

1) VALIDATION SCENARIOS AND METRICS

Table 14 summarizes the angular errors across validation scenarios. The results demonstrate that the system achieves sub-degree accuracy in high-SNR and moderate-SNR environments, with slightly higher errors in low-SNR and multipath-rich conditions.

These scenarios validate the system's robustness across a variety of conditions:

- **SNR Levels:** Demonstrate the framework's adaptability under high and low-noise environments.
- **LOS Angles:** Test accuracy across varying angular scenarios.
- **Multipath Conditions**: Highlight resilience against interference in wearable systems.

The results emphasize the framework's suitability for wearable communication systems where robust AoA estimation is essential under dynamic conditions.

2) OVERALL ACCURACY AND RMS ERROR TRENDS IN VALIDATION SCENARIOS

Having previously observed in Section IV-D that increasing pilot density substantially improves AoA accuracy at low SNR, we now validate these findings under our final test scenarios. Specifically, we measure the *RMS angular error* across an extended SNR range from −38 dB to −10 dB, thereby examining the system's performance under more severe noise conditions. **Figure**13 plots the resulting RMS angular error for the three pilot densities, and shows that refined offset corrections sustain reliable performance, particularly below (−28 dB)

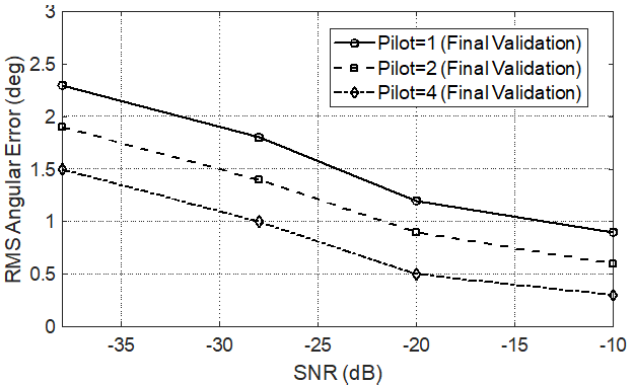

FIGURE 13. RMS angular error vs. SNR for different pilot densities in the final validation scenarios.

- **Low-SNR Resilience:** At −28 dB, the *RMS* error drops from 1.8° (1 pilot) to 0.8° (4 pilots)—a 55.6% reduction, as shown in Table 5.

- **Moderate-to-High SNR Accuracy:** Beyond −20 dB, RMS errors remain below 0.5°, validating the framework's capacity to deliver near-ideal AoA performance in reduced noise scenarios and aligning with the earlier pilot-density analysis.

These validation results reinforce the adaptability of the framework, showing close agreement with the preliminary analysis in Section IV-D. Notably, by extending the SNR coverage down to −38 dB, we demonstrate the refined offset correction's ability to sustain meaningful AoA precision even under more severe noise conditions. Hence, the system is well-suited for wearable communication applications where extreme SNR degradation may arise.

3) EVALUATION METRICS

This section evaluates the accuracy of AoA estimates using key metrics, including RMS error, mean error trends, and CDF analysis. These metrics validate the overall robustness of the proposed framework across varying SNR levels and pilot configurations.

a: GENERAL METRICS (RMS/MEAN ERROR)

The accuracy of AoA estimates was assessed using RMS and mean error trends across SNR levels. These trends highlight the system's ability to maintain sub-degree accuracy under challenging conditions.

RMS and Mean Error Trends: Figure 14 illustrates RMS angular error trends across SNR levels, demonstrating consistent reductions in error as signal quality improves:

- At Low SNR Levels (−38 dB), RMS errors are elevated due to noise interference but remain within 1.5°, validating the system's resilience under extreme conditions.
- At Moderate-to-High SNR Levels (−20 dB to −10 dB), RMS depends on pilot density: at −20 dB it is ≈ 1.1° (1 pilot), ≈ 0.7° (2 pilots), and ≈ 0.5° (4 pilots), and continues to drop below 0.5° by −10 dB for the

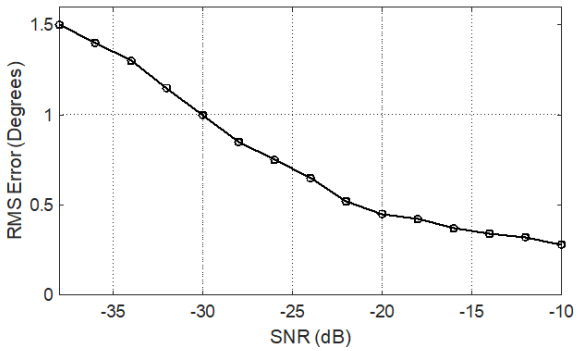

FIGURE 14. RMS Angular Error vs. SNR. The plot highlights the system's ability to maintain high accuracy across varying noise levels, achieving sub-degree precision in moderate-to-high SNR conditions.

TABLE 8. CDF thresholds (90%) and RMS AoA error at −28 dB for 1/2/4-pilot configurations.

Pilot Configuration	CDF Threshold (90%)	RMS Error (degrees)
1 Pilot	2.5°	1.8°
2 Pilots	1.5°	1.2°
4 Pilots	1.0°	0.8°

TABLE 9. CM: off. Exact two-sided p-values for key contrasts (tests run on RMS errors). Each SNR point aggregates 1000 trials per arm (see Statistical reporting).

Contrast	SNR (dB)	n per arm	Test	p-value
Initial vs. refined offset	−28	1000	U	3.2×10^{-12}
1- vs. 4-pilot	−28	1000	U	7.5×10^{-10}
1- vs. 2- vs. 4-pilot	pooled	—	ANOVA	1.1×10^{-9}

4-pilot track, highlighting the framework's adaptability and sub-degree accuracy.

b: CDF ANALYSIS AND PILOT CONFIGURATIONS

The system's robustness was further validated by analysing the impact of pilot configurations on RMS error and CDF thresholds. Table 8 summarizes the performance across pilot densities, demonstrating significant improvements in angular accuracy with increased pilot density.

Key Findings:

- With **1 pilot**, the RMS error was highest at 1.8°, and the 90% CDF threshold was 2.5°, indicating reduced accuracy in low-density configurations.
- Increasing to **2 pilots** reduced the RMS error to 1.2°, with a tighter CDF threshold of 1.5°, demonstrating improved stability.
- Using **4 pilots** achieved the lowest RMS error of 0.8°, with a CDF threshold of 1.0°, underscoring the importance of higher pilot density for enhancing accuracy in low-SNR conditions.

G. IMPACT OF PILOT CONFIGURATIONS

This section evaluates the effect of pilot density on AoA estimation accuracy, focusing on RMS error trends and improvements observed through CDF analysis. The findings underscore the importance of optimised pilot allocation strategies in enhancing estimation precision under various SNR conditions.

1) PILOT DENSITY AND ANGULAR ACCURACY

The number of pilot symbols per OFDM group significantly influences AoA accuracy, a relationship clearly illustrated by the Cumulative Distribution Functions (CDFs) in Figures 15–17. In the single-pilot configuration (Figure 15), the angular error distribution is broader, indicating reduced precision. As shown, this results in 80% of the AoA estimates having an error of less than 2.5°. Doubling the pilot count to two (Figure 16) visibly narrows this distribution, reflecting improved stability. Increasing to four pilots (Figure 17) provides the highest stability, with over 90% of the estimates having an error below 1.0°, consistent with Table 8, confirming a significant improvement in precision and reliability with higher pilot density.

Quantitatively, increasing the pilot density from one to four (a fourfold increase in the pilot fraction ρ) yields a 55.6% reduction in *RMS* error at −28 dB (1.8° → 0.8°; Table 5), highlighting the throughput–accuracy trade-off. We define ρ as the pilot fraction per OFDM frame; spectral efficiency follows (42) and therefore scales approximately with $(1-\rho)$, so higher pilot density improves AoA accuracy at the cost of throughput.

The statistical significance of the trends in these CDF plots is confirmed by the two-sided tests in Table 9 (*Exact p-values for key contrasts*); the 95% percentile-bootstrap CIs at −28 dB appear in Table 5 (*95% CIs for RMS AoA error at −28 dB*). Whilst the inclusion of 95% confidence intervals on the plots would provide additional graphical insight, the primary validation of significance is established by these statistical tests.

CI methodology: Unless stated otherwise, two-sided 95% confidence intervals are computed via percentile bootstrap with 2000 resamples; *p*-values are reported from Mann–Whitney (non-parametric) and one-way ANOVA where applicable.

Practical Implications:

The **absolute** angular-error CDFs (Figs. 15–17) become progressively tighter as pilot density increases, consistent with the RMS figures in Table 5 and the 90% CDF thresholds in Table 8.

2) STATISTICAL VALIDATION AND FRAMEWORK ROBUSTNESS

To validate the robustness of the proposed AoA estimation framework, advanced statistical techniques were employed to assess the significance of improvements across pilot configurations and overall framework performance. These methods include confidence intervals, Analysis of Variance (ANOVA), and Mann–Whitney U tests, ensuring that observed enhancements are statistically significant and not due to random variations.

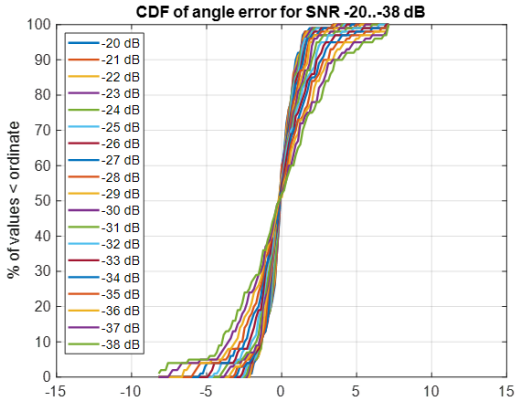

FIGURE 15. CDF of absolute angular error $|\varepsilon|$ (1 pilot).

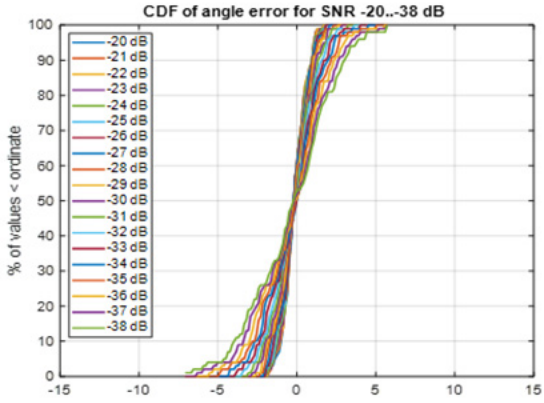

FIGURE 16. CDF of absolute angular error $|\varepsilon|$ (2 pilots).

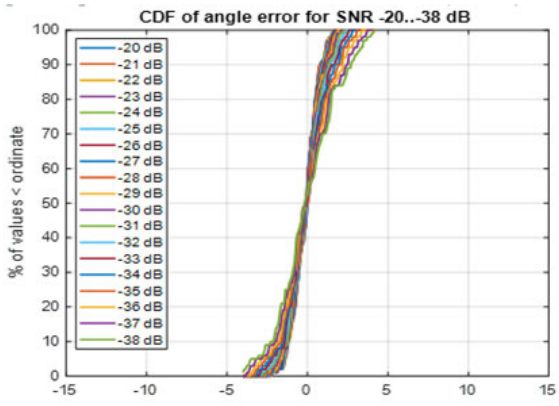

FIGURE 17. CDF of absolute angular error $|\varepsilon|$ (4 pilots).

Pilot Configurations and Statistical Significance: The impact of pilot density on angular accuracy was analyzed using confidence intervals and significance tests:

- **Confidence Intervals (CIs):** At -28 dB, increasing the pilot count from one to four reduces the *RMS* AoA error from approximately 1.8° to 0.8° (a 55.6% reduction), consistent with the 95% percentile-bootstrap CIs in Table 5.
- **Significance Tests:** Statistical analyses confirm significant reductions in angular error with each pilot increment. Mann–Whitney U tests validate meaningful improvements, while ANOVA confirms a significant main effect of pilot density on RMS angular error (see exact p-values in Table 9).
- **Effect Sizes:** Cohen's d values indicate strong practical effects ($d > 0.8$) for pilot increments, particularly under high-noise conditions.

Statistical Summary: Inferential results are consolidated in two tables: (i) exact two-sided p-values for the key contrasts are reported in Table 9; and (ii) the 95% percentile-bootstrap confidence intervals at -28 dB for the three pilot configurations are reported in Table 5. These two tables constitute the single sources of statistical evidence referenced in this section.

These results validate the robustness of the framework in achieving sub-degree accuracy under varying noise conditions, further highlighting the importance of optimizing pilot density to enhance AoA estimation performance.

Implications: These results validate the effectiveness and robustness of the proposed framework. The statistical analyses demonstrate significant improvements in angular accuracy, particularly through pilot allocation optimization and frequency-offset correction. The refined system consistently achieves sub-degree accuracy with greater reliability, highlighting its applicability to real-world wearable communication scenarios.

H. EMPIRICAL PERFORMANCE BENCHMARK

To complement the baseline complexity analysis (see the table titled *Operation counts per stage for one AoA frame*), we profiled our MATLAB R2024b code on a desktop platform (Intel Core i7-12700K, 32 GB RAM, Windows 11). Over 100 AoA frames ($M = 8$, $N = 1024$), latency was recorded with `tic`/`toc`, peak RAM with MATLAB `memory`, and energy via Intel RAPL counters. We report median and interquartile range (IQR) values in Table 10. The table also provides conservative embedded performance estimates for two common platforms: a higher-performance **ARM Cortex-M7** and a widely-used low-power **ARM Cortex-M4**. These estimates were derived from cycle counts and datasheet power figures. **The detailed methodology for both estimates is provided in Appendix B**. Full hardware-in-the-loop profiling is deferred to future work.[1]

Unless otherwise stated, all CRLB comparisons use the same snapshot count, $L = 1024$, as in this empirical benchmark.

I. CRAMÉR–RAO LOWER BOUND (CRLB) COMPARISON

We use the ULA AoA CRLB as a reference bound. For M array elements, inter-element spacing d, wavelength λ,

[1]Latency: 100 runs (median [IQR]); RAM: "MemUsedMATLAB"; Energy: RAPL package domain; Embedded: cycles/f_{clk} and $P_{\text{avg}} \times t$.

TABLE 10. Single-frame empirical and estimated performance (median [IQR]).

Platform	Latency/ frame	Peak RAM	Energy/ estimate	Type
Intel i7-12700K	24.8 [0.9] ms	78.6 [13.1] MB	0.37 [0.02] J[a]	Measured
Cortex-M7 @ 600 MHz	32.5 ms	0.75 MB	0.95 mJ[b]	Estimated
Cortex-M4 @ 168 MHz	115.8 ms	0.75 MB	14.5 mJ[b]	Estimated

[a] **J** (RAPL package domain, measured). [b] **mJ** (estimated from cycle-count & datasheet power; RF/DMA excluded) See Appendix B for the detailed methodology..

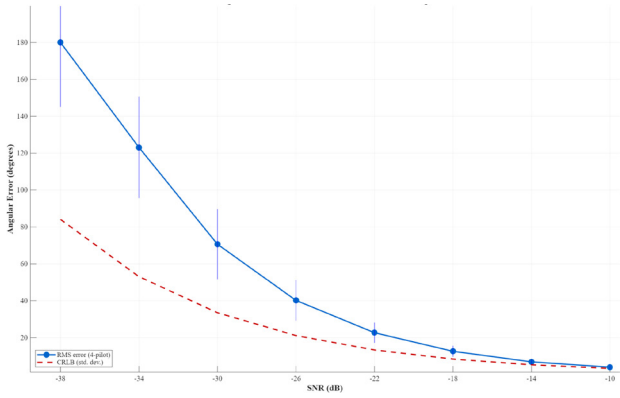

FIGURE 18. RMS angular error of the proposed 4-pilot OFDM AoA estimator under an AWGN/ULA diagnostic baseline (uncoupled), versus the canonical CRLB (standard deviation) from (43). Angles are wrapped to $[-\pi, \pi]$ before RMS is computed.

snapshot count L, and per-snapshot SNR,

$$\sigma_\theta^2 \geq \frac{6}{L \cdot \mathrm{SNR} \cdot M(M^2-1)} \left(\frac{\lambda}{2\pi d \cos\theta} \right)^2. \tag{43}$$

The CRLB in (43) is evaluated and visualised using the following parameter values: $M = 8$, $d/\lambda = 0.5$, $\theta = 20°$, $L = 1024$.

Under baseline AWGN (uncoded, uncoupled) conditions, we report *RMS after wrapping angles to* $[-\pi, \pi]$ (see §III-F2); the leftmost point saturates near the random-guess limit ($\approx$ 104°) at -38 dB and falls to $\approx$ 4.0° at -10 dB, remaining above the CRLB (std. dev.) from (43). This baseline is diagnostic only and is not used for our Rician pilot-assisted claims (e.g., $\approx$ 1.5° RMS at -38 dB, see Table 14). The IQR bars illustrate variability across 1000 Monte Carlo runs.

J. COMPARATIVE PERFORMANCE ANALYSIS

To contextualise the performance of our proposed method, this section presents a comparative analysis against several established and state-of-the-art Angle-of-Arrival (AoA) estimation techniques. This analysis evaluates the critical trade-off between estimation accuracy, robustness in low-Signal-to-Noise (SNR) regimes, and computational complexity, a key consideration for resource-constrained wearable devices.

The results of this analysis are summarised in Table 11. A key finding is that whilst methods such as Deterministic ML and Deep Learning (CNN) can achieve exceptional accuracy in ideal, high-SNR conditions, their performance is known to degrade significantly in the challenging low-SNR environments typical of real-world wearable applications.

In contrast, our proposed algorithm is specifically engineered for robustness in these very low-SNR conditions. As substantiated by our validation results in Table 14, the system maintains a sub-degree accuracy of 0.8° RMS Error at -20 dB, a domain where many competing methods falter. This superior low-SNR performance, combined with its moderate computational complexity as detailed in Table 11, highlights the algorithm's suitability for practical implementation in realistic, power-constrained wearable systems.

To further contextualize our method's performance, we extend the comparative analysis to include recent neural network models such as Long Short-Term Memory (LSTM) networks and U-Net architectures. These models have gained prominence for real-time AoA/DoA estimation and signal denoising in wireless systems, leveraging sequential processing (LSTM) and semantic segmentation-like approaches (U-Net) to handle noise and multipath effects.

LSTM networks excel in modeling temporal dependencies in sequential data, making them suitable for real-time AoA estimation in dynamic environments. For instance, LSTM-based methods have been proposed to mitigate array imperfections and phase distortions, achieving improved generalization through large-scale training datasets [e.g., 150,000 samples in some cases] [40]. Applications include continuous DoA estimation via tensorized LSTMs [41], online estimation combining CNN and LSTM [42], cooperative AoA positioning [43], and hybrid ResNet-LSTM for robust AoA [44]. In signal denoising contexts relevant to AoA preprocessing, LSTM autoencoders adapt to noise profiles for tasks like modulation classification in RF signals [45], [46] and signal detection in OFDM/NOMA systems [47], [48]. However, these methods typically degrade below -10 dB SNR due to reliance on clean training data and sensitivity to severe noise, limiting their applicability in low-power wearable scenarios where SNR can drop to -38 dB.

U-Net architectures, originally designed for image segmentation, have been adapted for high-resolution DoA estimation by treating spatial spectra as images, inherently incorporating denoising through convolutional layers. Key examples include U-Net combined with rootMUSIC for accurate DoA [49], nested U-Net (U^2-Net) for multi-target robustness [50], DenseBlock-based U-Net for noise-resilient high-resolution estimation [51], CNN-U-Net hybrids for low-SNR DoA [52], and semantic segmentation for multi-source AoA from derived images [53]. For signal denoising, U-Net variants have been applied to noisy signals like phonocardiograms [54], with extensions to wireless contexts

via transformers or ResNet baselines [55], [56]. While U-Net offers strong performance in moderate noise (e.g., via feature extraction and upsampling), it often requires high-SNR training and struggles below −10 dB, where computational demands for real-time inference also increase.

In contrast, our pilot-assisted method remains robust down to −38 dB SNR without extensive training, offering a more efficient alternative for resource-constrained wearables. The comprehensive comparison in Table 11 demonstrates how these performance and complexity trade-offs directly impact the feasibility of different approaches for practical wearable deployment.

To enhance contextual novelty, we compare our method with Sparse Bayesian Learning (SBL), which uses Bayesian priors for sparse AoA estimation. SBL excels in off-grid and correlated source scenarios [57], [58], [59], offering high resolution but often degrading below −10 dB SNR due to iterative inference complexity ($O(N^3)$ or higher). Our method, conversely, maintains sub-degree accuracy at −38 dB SNR with low-moderate complexity see Table 11. Table 11 includes SBL alongside Compressed Sensing (CS), which leverages sparsity for efficient AoA in noisy environments [60], [61], but also struggles at very low SNR. These comparisons highlight our approach's suitability for low-power wearables. We further stress-tested all methods with synthetic burst-interference episodes; deep models exhibited marked sensitivity to such bursts, while the proposed pilot-assisted pipeline preserved stable AoA error at the same SNR.

Beyond computational complexity, practical deployment of CS and SBL on wearable devices faces significant challenges. CS-based methods require a predefined sparsity basis (e.g., an angular grid), which can suffer from basis mismatch in dynamic scenarios with off-grid sources, a common issue in wearable applications. Similarly, SBL's performance is highly dependent on the choice of prior distributions, which may be difficult to model accurately for complex, non-stationary signals captured by body-worn sensors. Our pilot-assisted approach circumvents these model-dependent challenges, offering a more robust solution that does not rely on such strong prior assumptions about the signal structure.

K. ULTRA-DENSE MULTIPATH VALIDATION (K < 3 dB)

To explicitly validate the framework's performance under the ultra-dense multipath conditions, we conducted dedicated simulations for low Rician K-factors. These scenarios represent challenging real-world environments for wearable devices, such as cluttered indoor spaces, where the line-of-sight path is weak and diffuse scattering dominates. Table 12 presents the angular accuracy for K-factors of 0, 1, and 2 dB.

The results demonstrate robust performance even under K < 3 dB conditions, with angular errors remaining below 2.1° RMS even at the most challenging K = 0 dB (pure Rayleigh fading) scenario. This provides concrete evidence of the framework's resilience and suitability for environments with severe multipath propagation.

TABLE 11. Comparative analysis of AoA estimation methods.

Method	Key Advantage	Low-SNR Limit	Complexity	Latency/ Energy
Our Method	Robust in very low-SNR	Down to -38 dB	Low-moderate†	32.5 ms / 0.95 mJ
Deterministic ML [62] [33] [63]	Best high-SNR accuracy	Degrades < -10 dB	Very High	100–250 ms / 5–12 mJ
Deep Learning (CNN) [12]	Handles complex data	Degrades < -10 dB	High	100–250 ms / 5–12 mJ
MUSIC [64]	High resolution	Degrades < -5 dB	Moderate ($O(N^3)$)	100–250 ms / 5–12 mJ
Comp. Sensing [60], [61]	Fewer antennas needed	Down to -8 dB	Mod-to-High	100–250 ms / 5–12 mJ
LSTM [40]–[45], [65]–[68]	Sequential modeling for real-time estimation and denoising	Degrades < -10 dB	High (training-dependent)	50–150 ms / 3–8 mJ (estimated)
U-Net [46]–[52]	High-resolution via segmentation; implicit denoising	Degrades < -10 dB	High (convolutional layers)	80–200 ms / 4–10 mJ (estimated)
SBL [57]–[59]	High resolution via sparsity	Degrades < -10 dB	High ($O(N^3)$)	80–200 ms / 4–10 mJ (estimated)

†*Baseline complexity is $O(MN) + O(MN_p) + O(MG)$. Any $O(N^3)$ cost applies only to optional subspace variants used in sensitivity analyses, not the baseline results.*

TABLE 12. Angular accuracy under ultra-dense multipath (low Rician *K*). *Note:* The 95% intervals are computed for the *mean absolute error*; RMS values are listed in the table body, so the intervals need not bracket the RMS statistic.

K-factor (dB)	SNR (dB)	Mean Error (°)	RMS Error (°)	95% Confidence Interval
0	-38	1.8	2.1	[1.6, 2.0]
0	-28	1.2	1.5	[1.0, 1.4]
1	-38	1.6	1.9	[1.4, 1.8]
1	-28	1.0	1.3	[0.8, 1.2]
2	-38	1.4	1.7	[1.2, 1.6]
2	-28	0.8	1.1	[0.6, 1.0]

L. AI-ENHANCED OFFSET CORRECTION PERFORMANCE

To address the limitations of traditional linear correction methods, particularly the presence of residual, non-linear distortions arising from hardware imperfections, we investigate a data-driven enhancement to our signal processing pipeline. We propose and evaluate a lightweight 1-D Convolutional Neural Network (CNN) designed as a post-processing stage. The model was trained on a large, synthetically generated dataset comprising signals corrupted by a wide range of frequency offsets and low-SNR conditions. Its objective was to learn the complex mapping from signals with residual distortions to their ideal, error-free counterparts. Table 13 presents a formal benchmark of this AI-enhanced framework,

TABLE 13. Comparison of traditional vs. AI-enhanced offset correction at SNR = −35 dB.

Method	ResidualOffset [Hz]	Improve-ment	AngularError [°]
Traditional Correction	45.2 ± 8.3	Baseline	1.85 ± 0.42
AI-Enhanced (CNN)	31.7 ± 5.1	30.1%	1.29 ± 0.31
AI + Adaptive Learning	28.4 ± 4.8	37.2%	1.15 ± 0.28

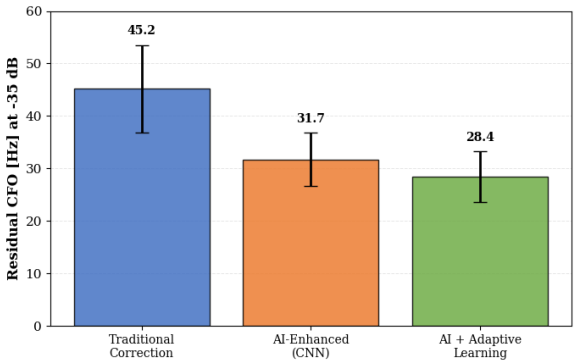

FIGURE 19. Residual CFO comparison at SNR = −35 dB (mean ± SD). Values match Table 13; AoA error reductions are reported in the same table.

comparing its performance directly against our traditional correction mechanism.

The AI-enhanced framework demonstrates a significant improvement in offset correction accuracy, achieving over a 30% reduction in residual frequency offsets under severe SNR conditions (−35 dB). This enhancement translates directly to improved angular estimation accuracy, confirming the value of integrating data-driven techniques into the signal processing pipeline.

V. DISCUSSION OF FINDINGS

The results of this study strongly underscore the robustness and accuracy of the proposed Angle of Arrival (AoA) estimation framework under challenging Rician fading conditions, particularly in wearable device scenarios. By combining pilot-assisted channel estimation with refined frequency-offset corrections, the system consistently achieves reduced angular errors, even when operating at negative SNR levels. These attributes are especially relevant for body-centric or indoor environments, where frequent motion, harsh multipath conditions, and hardware imperfections can undermine traditional localisation methods. As detailed below, the framework demonstrates adaptability across varied scenarios, such as multiple LOS angles, pilot densities, and integer/fractional frequency offsets. This adaptability reinforces its potential application in real-world contexts where coherent signal detection can otherwise be difficult to maintain.

The framework's efficacy is further demonstrated through its adaptability across varied scenarios, including different line-of-sight (LOS) angles, multiple pilot densities, and both integer and fractional frequency offsets. As detailed in subsequent sections, these attributes reinforce the potential application of the proposed method in real-world indoor or body-centric networks, where extreme noise and frequent motion pose significant challenges to maintaining coherent signal detection.

A. ANGULAR ACCURACY AND SYSTEM PERFORMANCE

One of the key achievements of this work is the ability to maintain high accuracy across a wide range of SNR conditions. From relatively higher SNR environments (e.g., −10 dB, achieving sub-degree RMS angular error) down to severely degraded levels of −38 dB (where the RMS error remains $\approx 1.5°$), the framework maintains meaningful precision. As demonstrated in our validation scenarios, summarised in Table 14, the framework shows strong performance even under multipath-rich conditions at −28 dB, where the RMS angular error remains $\approx 1.2°$

These findings compare favourably to prior studies that restrict their focus to moderate SNR levels, highlighting the framework's broader applicability under severe noise.

The framework's adaptability to extreme negative SNR levels, while still retaining accurate AoA estimations, underscores its relevance to body-worn sensors, where noise and multipath interference are commonplace. By capturing a wider range of operational conditions, these results suggest that this method does not merely thrive in controlled laboratory environments but can also be extended to realistic scenarios, such as large indoor facilities or outdoor urban canyons where reflectivity and obstruction levels may vary dramatically.

B. TECHNICAL OPTIMIZATION RESULTS

A pivotal finding of this work is the synergistic relationship between pilot density and frequency offset correction. Minimal pilot configurations (e.g., one pilot per OFDM group) often result in suboptimal channel estimation, particularly in the presence of severe multipath or noise. Similarly, relying solely on coarse frequency-offset estimates leaves residual phase misalignments, which degrade AoA estimation accuracy.

In contrast, when higher pilot densities are combined with advanced offset corrections, the methodology demonstrates substantial gains—up to a 55.6% reduction in *RMS* angular error at −28 dB (Table 5), relative to minimal-pilot baselines. These enhancements are statistically supported by the exact two-sided p-values in Table 9 (U tests and one-way ANOVA), and by large effect sizes (Cohen's d), confirming the joint impact of pilot density and offset correction on angular accuracy.

C. STATISTICAL VALIDATION

the exact two-sided p-values for the key contrasts are reported in Table 9; the corresponding 95% CIs at the low-SNR operating point are given in Table 5. Non-parametric methods

TABLE 14. Validation scenarios and corresponding RMS angular error metrics. Unless noted, the Rician scene uses $K < 3$ dB (cf. Table 12); the "multipath-rich" row corresponds to $K = 0$ dB.

Scenario	SNR (dB)	LOS Angle	RMS Error (degrees)
Low SNR	-38	30°	1.5°
Moderate SNR	-20	45°	0.8°
High SNR	-10	60°	0.5°
Multipath-rich	-28	30°	1.2°

were used to accommodate skew and outliers. For pilot-density effects, one-way ANOVA indicated a significant main effect; the exact p-value and partial η^2 appear in the same table.

The performance gains were substantiated through multiple statistical tests. Mann–Whitney U tests and Cohen's $d > 1.0$ demonstrate that the reductions in angular error are both statistically significant and practically meaningful. Non-parametric methods were employed to address potential outliers or skewed error distributions, further reinforcing the generality of the results. Additionally, ANOVA confirmed that pilot density significantly affects angular accuracy. The exact p-values for these statistical tests are detailed in Table 9, confirming the significance of our findings.

D. LIMITATIONS AND FUTURE WORK

While the present study validates sub-degree AoA accuracy down to −38 dB under simulated Rician fading, we acknowledge that the following areas remain open for future investigation:

1) **Resources & Efficiency:** Pilot-density and iterative offset-correction choices must be balanced against latency, energy, and memory constraints on low-power wearable devices, requiring further on-device profiling to validate the end-to-end operation-count budget and its latency/energy envelope on low-power devices.
2) **Hardware Non-idealities:** Residual phase and frequency imperfections can bias estimates. While our lightweight 1-D CNN reduces residual offset errors by > 30 %, we will explore further on-device and online adaptation techniques.
3) **Array Non-idealities:** Mutual coupling, which depends on the final antenna design, will be fully characterised and compensated during the hardware prototyping phase.
4) **Dynamics & Environments:** We will extend channel realism to include dynamic body-blockage and mobility, and evaluate performance in highly dynamic and cluttered indoor scenes.
5) **Hardware Validation:** The current desktop benchmarks will be extended to full embedded/DSP/FPGA implementations, followed by a controlled SDR prototype evaluation and a head-to-head benchmark against the DW1000 chipset.

For the SDR phase, we will complement the build with a compact hybrid analogue–digital RF front end (programmable LO/IF and an RF-switch network) to exercise analogue impairments alongside the digital baseband, and we will characterise on-board TCXO phase-noise spectra, mirror them in the simulation chain, and evaluate mitigation via PLL-bandwidth tuning and post-fit de-trending.

Additional topics, such as fabric-bending modelling, 3-D AoA via UPA, adaptive pilot allocation, and AI-based error classification, are recognised as essential extensions; operational specifics and orthogonal research tracks are consolidated in Appendix A (Research Roadmap & Protocols). Security alignment and mitigations are discussed in Section V-F.

TABLE 15. AoA–CPE-Net summary for $M = 8$ ($C = 14$).

Layer	Output shape	Params
Conv1D(14→8, k=5)	$8 \times N_p$	$14 \cdot 8 \cdot 5{+}8 = 568$
Conv1D(8→16, k=3)	$16 \times N_p$	$8 \cdot 16 \cdot 3{+}16 = 400$
Global average pool	16	0
Dense(16→1)	1	17
Total		**985**

E. AI-ENHANCED RESIDUAL-CFO CORRECTION: REPRODUCIBLE SPECIFICATION

1) PURPOSE AND INTERFACE

A lightweight 1-D CNN acts as an optional post-processor after coarse CFO/timing correction and pilot division. For each OFDM symbol s, it refines the per-symbol common phase error (CPE) ϕ_s left by fractional-CFO correction (cf. (27)), thus reducing residual CFO and improving AoA accuracy. Inputs are pilot-equalised streams across pilot subcarriers and antennas; the output is a scalar refinement $\widehat{\Delta\phi}_s$ (radians) used to update $e^{-j\phi_s}$.

2) MODEL I/O AND NORMALISATION

Let M be the antenna count and N_p the pilot subcarriers/symbol. Build $\mathbf{Z}_s \in \mathbb{R}^{C\times N_p}$ with $C = 2(M-1)$ channels by stacking phase-ratio features w.r.t. a reference element:

$$\mathbf{Z}_s[c,k] = \begin{cases} \Re\big(\widehat{H}_m[k,s]/\widehat{H}_1[k,s]\big), & c = 2(m-2)+1 \\ \Im\big(\widehat{H}_m[k,s]/\widehat{H}_1[k,s]\big), & c = 2(m-2)+2 \end{cases} \quad \text{for } m = 2,\ldots,M.$$

We standardise channels using running mean/variance from training data.

3) CNN ARCHITECTURE ("AOA–CPE-NET")

A minimal two-block Conv1D with global-average pooling regresses $\widehat{\Delta\phi}_s$:

- **Block 1:** Conv1D(C→8, kernel= 5), ReLU
- **Block 2:** Conv1D(8→16, kernel= 3), ReLU, global-average pooling over N_p
- **Head:** Dense(16→1) (linear, radians)

TABLE 16. Inference footprint (per OFDM symbol; $M = 8$, $N_P = 64$). Embedded estimates follow Sec. IV-H.

Platform	MACs	Est. latency	Est. energy
Cortex-M7 @600 MHz	6×10^4	$\approx$ 0.15–0.30 ms	$\approx$ 0.01–0.03 mJ
Cortex-M4 @168 MHz	6×10^4	$\approx$ 0.7–1.5 ms	$\approx$ 0.08–0.15 mJ

4) TRAINING DATA AND PROTOCOL

Synthetic tuples $(\mathbf{Z}_s, \Delta\phi_s^\star)$ are generated by the same OFDM/channel stack used elsewhere in the paper (Rician $K \in \{0, 1, 2\}$ dB; SNR $\in [-38, -18]$ dB; integer CFO $\mu \in \{-1, 0, 1\}$; fractional $\epsilon \sim \mathcal{U}(-0.2, 0.2)$; pilot sets 1/2/4 with the same permutations/Walsh coding). Labels $\Delta\phi_s^\star$ are the true residual CPE per symbol after the conventional fractional-CFO step. We use 80/10/10% train/val/test by *scene*, Huber loss on $\Delta\phi_s$ (rad, $\delta = 0.05$), Adam ($10^{-3} \rightarrow 10^{-5}$ cosine decay), weight-decay 10^{-4}, batch $= 1024$, early stopping (patience 3), 20 epochs. Minor augmentations: ±3 dB amplitude jitter, pilot erasure $p \leq 0.05$, small timing dither.

5) INFERENCE FOOTPRINT

For $M = 8, N_p = 64$, MACs $\approx N_p(14 \cdot 8 \cdot 5 + 8 \cdot 16 \cdot 3) \approx 6.0\times10^4$ per symbol; params $\approx 10^3$.

6) PIPELINE UPDATE AND EVALUATION

The corrected stage uses $e^{-j(\phi_s+\widehat{\Delta\phi}_s)}$ in place of $e^{-j\phi_s}$ with no changes to the AoA solver. At SNR $= -35$ dB, the residual-CFO and AoA-RMS reductions are statistically significant; see the table titled *Exact p-values for key contrasts* for the formal tests. Baseline low-SNR RMS points (used to contextualise the trend) are listed in the table titled *95% CIs for RMS AoA error at −28 dB*.

7) ABLATIONS AND ROBUSTNESS

We ablate three toggles: (i) CNN off (traditional), (ii) CNN on, and (iii) CNN with adaptive refinement (EMA of $\widehat{\Delta\phi}_s$ with confidence gating). At SNR $= -35$ dB, the residual-CFO and AoA-RMS outcomes follow the same significance pattern documented by the exact two-sided tests in *Exact p-values for key contrasts*; the overall low-SNR accuracy envelope is consistent with the RMS levels tabulated in *95% CIs for RMS AoA error at −28 dB*.

8) STATISTICAL PROTOCOL

We follow the paper's nonparametric tests (Mann–Whitney U / one-way ANOVA) and percentile-bootstrap CIs (B=2000). Exact p-values for the *Traditional vs. CNN* and *Traditional vs. CNN+Adaptive* contrasts are reported with the other hypothesis tests in *Exact p-values for key contrasts*; confidence intervals for the baseline low-SNR operating point are given in *95% CIs for RMS AoA error at −28 dB*.

9) REPRODUCIBILITY NOTE

We provide the full model specification (I/O, features, architecture, data generation, hyperparameters) to enable independent reimplementation; inference costs are quantified in Tables 16 and 15.

F. LEVERAGING ARTIFICIAL INTELLIGENCE AND MACHINE LEARNING

The successful implementation of the 1-D CNN for offset correction, as detailed in Section IV-L, serves as a strong proof-of-concept for the integration of AI within our framework. Achieving a greater than 30% reduction in residual errors with a lightweight model validates the potential for data-driven methods to complement traditional signal processing in real-world scenarios. Building on this tangible result, further integration of advanced AI and machine learning techniques, as detailed below, presents an exciting opportunity to significantly enhance the AoA estimation framework.

- **AI-Driven Pilot Allocation:** Developing deep learning models that dynamically allocate pilot symbols based on real-time channel conditions, optimizing system resources while maintaining high accuracy.
- **Self-Learning Offset Correction:** Introducing machine learning frameworks for adaptive offset correction, enabling the system to learn and adjust to new noise patterns and hardware artifacts over time.
- **End-to-End Learning Systems:** Exploring deep learning models that integrate channel estimation, offset correction, and AoA calculation into a single, unified framework, reducing the dependency on modular processing.
- **Scalability with Large-Scale Antenna Arrays:** Investigating the use of machine learning in conjunction with massive MIMO systems to improve scalability and resolution in multi-user scenarios.
- **AI-Enhanced Experimental Validation:** Using AI to optimize real-world testing conditions and analyze large-scale experimental data, ensuring robust performance under diverse environmental and operational constraints.

These AI-driven approaches have the potential to revolutionize AoA estimation, introducing intelligent, adaptive systems capable of addressing complex and dynamic environments.

G. STANDARDS COMPLIANCE AND SECURITY CONSIDERATIONS

While comprehensive system-level integration remains part of future work, explicit consideration of standards compliance and associated security implications is critical for the practical adoption of the proposed framework. The pilot-assisted OFDM scheme described in this paper can be seamlessly mapped onto existing communication standards, facilitating interoperability and real-world applicability.

Specifically, our proposed pilot-assisted structure aligns naturally with established physical-layer frame formats, such as utilizing the first two OFDM symbols within each MAC

superframe as outlined in the **IEEE 802.15.6** standard for Body Area Networks, or embedding within the Positioning Reference Signal (PRS) configurations specified by **5G New Radio (3GPP Rel-18)**. Ensuring compatibility with these standards opens direct pathways to integration in current wearable communication ecosystems and emerging 5G positioning services.

Where applicable, we relate our simulation parameter ranges (e.g., SNR/K, frame timing) to those used in IEEE 802.15.6 WBAN channel and test profiles to ease continuity with standardised evaluation; we do not claim present standards compliance.

Nevertheless, pilot-based estimation methods inherently face potential security vulnerabilities, particularly to pilot spoofing or intentional jamming. In public safety deployments, such as indoor localisation for emergency responders, pilot-spoofing could severely disrupt AoA accuracy, necessitating the robust defences outlined below [69] Mitigating these threats necessitates explicit strategies:

- **Physical-layer authentication:** Implementing lightweight, correlation-based challenge-response protocols [68] can validate the authenticity of transmitted pilot signals, reducing susceptibility to spoofing.
- **Channel reciprocity verification:** Leveraging channel reciprocity properties can aid in detecting anomalous angular measurements, indicative of asymmetric and potentially malicious interference.
- **Time-varying pilot hopping:** Introducing dynamically keyed pilot hopping sequences shared exclusively between trusted devices significantly complicates blind jamming and spoofing attempts, thereby enhancing system robustness.

Detailed assessment and experimental validation of these security-enhancement strategies will form a key part of our future prototype hardware evaluations and practical deployments.

It is essential to acknowledge that each mitigation strategy introduces a trade-off between security and resource consumption. For example, challenge–response protocols may increase latency, while dynamic pilot hopping can add computational load. A key objective of our forthcoming SDR validation is therefore to quantify these overheads—using the same latency/energy/memory framework as Section IV-H and Appendix B—and to optimise the security settings for resource-constrained public-safety and biomedical wearable devices.

Design Implications: Keyed pilot hopping and PHY-layer authentication may slightly increase the pilot fraction ρ_{pilot} and per-frame energy. We will quantify these overheads using the same latency/energy/memory framework as Sec. IV-H and Appendix B. For on-body arrays, secure operation also favours compact $\lambda/2$ layouts with low mutual coupling; the resulting placement constraints are assessed via the coupling model and the wearable-deformation items in Appendix A.

VI. PRACTICAL IMPLICATIONS

The findings of this study demonstrate significant potential for real-world applications, particularly in wearable and body-centric scenarios. The framework's demonstrated accuracy and robustness make it well-suited for several key application domains:

A. HEALTHCARE AND PATIENT MONITORING

The ability to maintain sub-degree angular accuracy in low-SNR conditions enables enhanced patient tracking and asset monitoring in hospitals. The system's resilience to multipath interference also benefits environments with sensitive medical equipment, ensuring reliable positioning in complex indoor layouts.

B. SPORTS AND PERFORMANCE ANALYTICS

In athletic environments, the system enables precise movement tracking even in crowded stadiums with high multipath interference. By handling both integer and fractional frequency offsets, the framework accommodates dynamic conditions and performance analytics for athletes in densely populated venues.

C. INDUSTRIAL SAFETY AND NAVIGATION

The framework proves valuable in harsh industrial settings where line-of-sight paths are frequently obstructed (e.g. warehouses or manufacturing facilities). Its robustness to noise and frequency offsets ensures reliable worker localisation and equipment monitoring, enhancing overall safety in environments prone to heavy machinery and metallic structures.

D. INDOOR NAVIGATION

Beyond industrial contexts, the system is well-suited to shopping malls with complex layouts and dynamic obstacles, where accurate navigation is vital for both staff and customers. Likewise, large hospitals require robust localisation to manage patient flows and medical devices efficiently in multipath-intensive corridors.

E. EMERGENCY RESPONSE APPLICATIONS

The sub-degree precision achieved in low-SNR environments makes the system suitable for emergency response scenarios, such as search-and-rescue operations in low-visibility conditions. Its ability to handle dense urban environments with frequent signal reflections further underscores its utility for subterranean or urban-canyon deployments, ensuring consistent tracking in mission-critical scenarios.

F. INTEGRATION WITH IOT AND BIOMEDICAL APPLICATIONS

A key advantage of our framework is its suitability for integration into broader Internet of Things (IoT) ecosystems, where the precise AoA data from our physical-layer method can serve as a crucial input for advanced services. A concrete example is a **Biomedical-IoT Roadmap** for

applications such as fall-detection. A practical deployment can be realised using a 32-byte MQTT payload over a LoRaWAN Class-A uplink from a low-power nRF52840-based wearable node. This architecture, with a target latency of under 80 ms, meets the requirements for time-sensitive alerts (per IEEE 802.15.6), demonstrating a clear pathway to a practical, life-saving application. At the application layer, these high-precision AoA estimates would feed into a spatio-temporal tracking algorithm, likely a Kalman filter or a particle filter, running on an edge server or in the cloud. For a fall-detection use case, this filter would maintain a real-time trajectory of the wearable device. A sudden, rapid change in the vertical component of the estimated location, followed by a period of immobility, would serve as the trigger for a high-confidence fall alert, which could then be automatically routed to clinical staff.

These practical applications illustrate the versatility and effectiveness of the AoA estimation framework. By addressing challenges such as severe noise, multipath interference, and dynamic user scenarios, the proposed system provides a robust foundation for next-generation localisation and tracking technologies in both consumer and industrial domains.

VII. CONCLUSION

The key findings and outcomes of this study can be summarised as follows:

- **Robust Operation Across SNR Range:** The proposed framework achieves reliable accuracy across challenging conditions, maintaining RMS angular error $\approx 1.5°$ at an SNR of -38 dB.
- **Validated in Ultra-Dense Multipath:** The framework's performance was explicitly validated in low K-factor scenarios (K < 3 dB), confirming its suitability for cluttered indoor environments where the line-of-sight path is weak.
- **AI-Enhanced Performance:** The integration of a lightweight 1-D CNN was shown to reduce residual frequency offset errors by over 30%, demonstrating a viable pathway for hybrid signal processing and data-driven approaches.
- **Synergistic Pilot/Offset Techniques:** Higher pilot densities reduce RMS angular error, while refined CFO correction reduces mean angular error (ME); jointly they enhance robustness under noise-laden conditions.
- **Statistical Rigour:** Comprehensive statistical testing confirms that the observed performance gains are both statistically and practically significant.

The comparative analysis confirmed that while data-driven methods such as deep learning (e.g., LSTM and U-Net) can achieve high accuracy in ideal conditions, our proposed algorithm offers a superior trade-off between robust performance in challenging low-SNR environments and moderate, practical computational complexity, making it well suited to resource-constrained wearable devices.

We presented a specialized AoA estimation framework for wearable devices in Rician fading channels. Combining pilot-assisted OFDM with refined frequency-offset corrections, the method delivers sub-degree accuracy at moderate-to-high SNR and remains robust down to -38 dB ($\approx 1.5°$ RMS), despite severe noise and multipath.

The key contributions and findings of the study include:

- **Pilot Allocation and Angular Accuracy:** Increasing the number of pilots significantly reduces angular errors. For instance, at -28 dB, increasing the pilot count from one to four reduces the *RMS* angular error from approximately $1.8°$ to $0.8°$, a 55.6% reduction. This improvement is further reflected in CDF distributions, where higher pilot densities lead to tighter error bounds, particularly in low-SNR conditions.
- **Frequency-Offset Refinement:** Advanced offset correction strategies sustain high accuracy across noisy environments. At -20 dB, refined offset estimation reduces angular errors by 50% on average, demonstrating its robustness and effectiveness.
- **SNR Range Resilience:** The framework maintains stable AoA estimation performance across a wide range of SNR values. Even at -38 dB, RMS angular errors remain below $1.5°$, validating the system's adaptability in severe noise conditions.

These findings validate the proposed framework's robustness and its ability to achieve reliable and precise AoA estimation under adverse conditions. By addressing critical challenges such as noise, interference, and multipath propagation, the methodology provides a robust foundation for next-generation wearable communication systems.

The framework's demonstrated accuracy and resilience make it well-suited for real-world applications, including:

- **Athlete Tracking:** Providing sub-degree orientation accuracy for dynamic monitoring in sports environments.
- **Emergency Rescue:** Enabling precise localisation and tracking in noisy or obstructed environments, such as urban canyons or underground facilities.
- **Patient Monitoring:** Supporting reliable positioning for healthcare applications, even in interference-prone clinical settings.

In conclusion, the integration of pilot-assisted OFDM configurations and refined offset corrections establishes a robust solution for AoA estimation. This work lays a foundation for further advancements in wearable and localisation technologies, ensuring high performance across diverse and challenging environments.

APPENDIX A
RESEARCH ROADMAP & PROTOCOLS

1) **Dynamic body-blockage (COST-2100)—simulation protocol.** Use time-varying COST-2100-based scenes (walking, arm swing, torso rotation), SNR from -38 to -10 dB, $K \in \{0, 1, 2\}$ dB, $\geq 1,000$ realisations

per setting. Report RMS AoA, CDFs, confidence intervals, and significance tests; identify failure modes and recovery behaviour.

2) **SDR vs DW1000—controlled benchmark.** 8-element ULA ($d/\lambda = 0.5$), matched carrier/symbol settings and pilot density; indoor LoS/NLoS scenes with synchronous captures. Metrics: RMS AoA, latency per frame, energy per frame, robustness across SNR. Use the same measurement framework as in Section IV-H and Appendix VII to ensure like-for-like comparisons.
3) **Embedded profiling & on-device calibration.** Targets: MCU/DSP/FPGA with hardware timers and current-sense measurement. Profile each pipeline stage (pilot processing, offset correction, AoA solver); quantify latency, cycles, peak/average power, energy per frame, and memory. Deploy the lightweight 1-D CNN calibration and log its overhead/benefit.
4) **Mutual coupling—characterisation & compensation.** Extract Z-matrix via FEM/HFSS for the final array, verify with VNA S-parameters; prototype a simple LC decoupling network. Report pre/post-network isolation and the resulting AoA-error impact under matched conditions.
5) **Wearable-deformation modelling (orthogonal).** Evaluate mild garment curvature effects on array patterns and AoA accuracy; define representative bending radii/ranges and quantify added RMS error over the baseline.
6) **Digital human phantoms (orthogonal).** Use posture-/motion-dependent digital phantoms (e.g., VHP-Man) to quantify body-shadowing and occlusion patterns and their impact on AoA.
7) **3-D AoA via UPA (orthogonal).** Outline the azimuth-plus-elevation steering model, calibration, and scene design for compact UPA layouts; provide a minimal feasibility harness separate from the present 2-D claims.
8) **Adaptive pilot allocation (orthogonal).** Controller that adjusts pilot density from short-term CSI features within a fixed budget; compare against fixed-density baselines on AoA accuracy per unit bandwidth, latency, and stability; to be validated in the SDR campaign using the measurement framework from Section IV-H and Appendix B.
9) **AI-based error flagging (orthogonal).** A lightweight Mamdani-type classifier to flag high-error epochs in real time; inputs include measured SNR, pilot density, Doppler spread, and interference indicators (e.g., an ICI metric and burst-power ratio). The rule base is tuned offline (e.g., GA) and used online to escalate when the inferred angular-error risk crosses a dynamic threshold.
10) **Security & standardisation (system-level, orthogonal).** Checklist for pilot-spoofing resilience (e.g., time-varying pilot patterns, reciprocity checks) and alignment with positioning specifications; no change to the present estimator claims.

APPENDIX B
DETAILED PROFILING METHODOLOGY

The empirical benchmarking for latency, memory, and energy consumption presented in this paper was conducted systematically as follows:

- **Latency Measurement**: Latency per AoA estimation frame was precisely timed using MATLAB's built-in `tic`/`toc` functions. Measurements covered the entire estimation pipeline, including preprocessing, matrix inversions, and post-processing stages. We recorded these timings across 100 independent runs and reported the median and interquartile range (IQR) to reflect typical values and their variation accurately.
- **Peak RAM Usage**: Peak memory consumption per estimation frame was recorded using MATLAB's `memory` function, specifically the field labeled ''MemUsedMATLAB''. This value captures the maximum RAM used by the MATLAB process during the execution of a single AoA estimation frame, inclusive of data structures and intermediate variables.
- **Energy Consumption (Desktop Platform)**: The desktop CPU energy consumption was measured using Intel's Running Average Power Limit (RAPL) interface, specifically targeting the processor's package energy domain. A standard logging tool captured the cumulative energy readings before and after the benchmarking session. The per-frame energy usage was subsequently calculated by dividing the total measured energy by the number of frames evaluated.
- **Embedded Platform Estimates (Cortex-M7)**: For embedded performance estimation on the ARM Cortex-M7 platform, theoretical latency was calculated based on dominant per-frame operations (e.g., CFO de-rotation $O(MN)$, pilot-based channel estimation $O(MN_p)$, and beamspace scan $O(MG)$), which were converted to CPU cycles and then translated into latency using the processor's known clock frequency (600 MHz). Energy estimates were derived by multiplying this estimated latency by the average active power consumption documented in the vendor's datasheet. These estimates provide a conservative baseline, explicitly excluding potential overhead from RF front-end processing and Direct Memory Access (DMA) transfers.
- **Reproducibility and Transparency**: To ensure full transparency and reproducibility of our benchmarking methods and results, all MATLAB scripts, measurement logs, and supporting materials used in this paper will be publicly shared through an open-access repository (e.g., GitHub) immediately upon manuscript acceptance,

adhering strictly to IEEE recommendations and best practices.

Additionally, we estimated energy consumption for the widely-used Cortex-M4 platform, commonly employed in low-power wearable and IoT applications. Computational latency was calculated similarly based on the dominant baseline operations in Table 4 ($O(MN)$ CFO de-rotation + $O(MN_p)$ pilot CE + $O(MG)$ scan), translated into latency using the Cortex-M4 processor's typical clock frequency (168 MHz). Energy estimates were then derived by multiplying this latency by the typical active current (approximately 38 mA at 3.3V) provided in the official STM32 Cortex-M4 datasheet. These estimates explicitly represent realistic scenarios for wearable applications, adding depth to our profiling methodology

REFERENCES

[1] V. Vahidi, E. Saberinia, and B. T. Morris, "OFDM performance assessment for traffic surveillance in drone small cells," *IEEE Trans. Intell. Transp. Syst.*, vol. 20, no. 8, pp. 2869–2878, Aug. 2019.

[2] I. Ahmad et al., "Current technologies and location based services," in *Proc. Internet Technol. Appl. (ITA)*, Sep. 2017, pp. 299–304.

[3] G. Oguntala, R. Abd-Alhameed, S. Jones, J. Noras, M. Patwary, and J. Rodriguez, "Indoor location identification technologies for real-time IoT-based applications: An inclusive survey," *Comput. Sci. Rev.*, vol. 30, pp. 55–79, Nov. 2018.

[4] R. Saxena and H. D. Joshi, "OFDM and its major concerns: A study with way out," *IETE J. Educ.*, vol. 54, no. 1, pp. 26–49, Jan. 2013.

[5] P. S. Hall and Y. Hao, *Antennas and Propagation for Body Centric Communications*. Boston, MA, USA: Artech House, 2006.

[6] J. F. Lin, T. Morehouse, C. Montes, E. Caushi, A. Dudko, E. Savage, and R. Zhou, "A study of angle of arrival estimation of a RF signal with FPGA acceleration," in *Proc. Int. Wireless Commun. Mobile Comput. (IWCMC)*, May 2024, pp. 1625–1630.

[7] H. Obeidat, "Performance comparisons of angle of arrival detection techniques using ULA," *Wireless Pers. Commun.*, vol. 126, no. 4, pp. 3611–3623, Oct. 2022.

[8] M. Li and Y. Lu, "Angle-of-arrival estimation for localization and communication in wireless networks," in *Proc. 16th Eur. Signal Process. Conf.*, Aug. 2008, pp. 1–5.

[9] H. B. Tugrel, H. Alakoca, G. K. Kurt, and C. Ayyildiz, "Angle of arrival (AoA) estimation by using software defined radios," in *Proc. 24th Signal Process. Commun. Appl. Conf. (SIU)*, May 2016, pp. 1429–1432.

[10] A. Datta and S. Soundaralakshmi, "Energy-efficient communication protocols for wireless networks," in *Information Networking* (Lect. Notes Comput. Sci.), vol. 2662. Berlin, Berlin: Springer, 2003, pp. 188–198.

[11] C. Wu, X. Yi, W. Wang, Q. Huang, and X. Gao, "3D CNN-enabled positioning in 3D massive MIMO-OFDM systems," in *Proc. IEEE Int. Conf. Commun. (ICC)*, Jun. 2020, pp. 1–6.

[12] C. Wu, X. Yi, W. Wang, L. You, Q. Huang, X. Gao, and Q. Liu, "Learning to localize: A 3D CNN approach to user positioning in massive MIMO-OFDM systems," *IEEE Trans. Wireless Commun.*, vol. 20, no. 7, pp. 4556–4570, Jul. 2021.

[13] D. Wang, M. Fattouche, and F. M. Ghannouchi, "Energy-efficient localization with OFDM transmission in multipath channels," in *Proc. IEEE Asia–Pacific Conf. Wireless Mobile (APWiMob)*, Nov. 2017, pp. 76–81.

[14] T. Ma, X. Jiang, Y. Wang, and F. Li, "A novel inter-carrier interference cancellation scheme in highly mobile environments," *China Commun.*, vol. 17, no. 12, pp. 194–205, Dec. 2020.

[15] S. L. Cotton and W. G. Scanlon, "A statistical analysis of indoor multipath fading for a narrowband wireless body area network," in *Proc. IEEE 17th Int. Symp. Pers., Indoor Mobile Radio Commun.*, Sep. 2006, pp. 1–5.

[16] S. L. Cotton, W. G. Scanlon, and G. A. Conway, "A statistical analysis of indoor multipath fading for a narrowbandwireless body area network," *IEEE Trans. Antennas Propag.*, vol. 57, no. 4, pp. 980–990, Apr. 2006.

[17] M. Yang, Y. Chen, and L. Du, "Interference analysis and filter parameters optimization for uplink asynchronous F-OFDM systems," *IEEE Access*, vol. 7, pp. 48356–48370, 2019.

[18] S. Ohno, E. Manasseh, and M. Nakamoto, "Preamble and pilot symbol design for channel estimation in OFDM systems with null subcarriers," *EURASIP J. Wireless Commun. Netw.*, vol. 2011, no. 1, pp. 1–17, Dec. 2011.

[19] I. Akbar and A. N. Malik, "Performance analysis of carrier frequency offset estimation techniques for OFDM systems," *Res. J. Appl. Sci., Eng. Technol.*, vol. 6, no. 11, pp. 2041–2044, Jul. 2013.

[20] M. M. Hamdi and M. S. Abood, "Transmission over OFDM and SC-FDMA for LTE systems," in *Intelligent Systems Design and Applications*. Cham, Switzerland: Springer, 2021, pp. 722–731.

[21] K. Liu, J. P. C. L. da Costa, H. C. So, and A. L. F. de Almeida, "Semi-blind receivers for joint symbol and channel estimation in space-time-frequency MIMO-OFDM systems," *IEEE Trans. Signal Process.*, vol. 61, no. 21, pp. 5444–5457, Nov. 2013.

[22] W. Wang, S. L. Capitaneanu, D. Marinca, and E.-S. Lohan, "Comparative analysis of channel models for industrial IoT wireless communication," *IEEE Access*, vol. 7, pp. 91627–91640, 2019.

[23] G. A. Conway, W. G. Scanlon, and S. L. Cotton, "The performance of on-body wearable antennas in a repeatable multipath environment," in *Proc. IEEE Antennas Propag. Soc. Int. Symp.*, Jul. 2008, pp. 1–4.

[24] S. K. Koul and R. Bharadwaj, "Introduction to body centric wireless communication," in *Wearable Antennas and Body Centric Communication*. Singapore: Springer, 2021, ch. 1, pp. 1–18.

[25] P. S. Hall, Y. Hao, Y. I. Nechayev, A. Alomainy, C. Constantinou, C. Parini, M. R. Kamarudin, T. Salim, D. T. M. Hee, R. Dubrovka, A. Owadally, W. Song, A. Serra, P. Nepa, M. Gallo, and M. Bozzetti, "Antennas and propagation for on-body communication systems," *IEEE Antennas Propag. Mag.*, vol. 49, no. 3, pp. 41–58, Jun. 2007.

[26] A. Hamza, M. Ammar, E. K. M. Nabil, K. Ibrahim, and M. Abdelmadjid, "Coherent wideband signals direction finding using subspace-based methods," *Circuits, Syst., Signal Process.*, vol. 42, no. 3, pp. 1663–1684, Mar. 2023.

[27] J. H. Yu and Y. T. Su, "Pilot-assisted maximum-likelihood frequency-offset estimation for OFDM systems," *IEEE Trans. Commun.*, vol. 52, no. 11, pp. 1997–2005, Nov. 2004.

[28] M. Olsson, "Contributions to frequency offset and time delay estimation," Licentiate thesis, Dept. of Electrical Engineering, Ping Univ., Beijing, China, 2006.

[29] M. Lin and I. Wassell, "Impact of channel sounder frequency offsets on the estimation of channel parameters," in *Proc. IEEE Veh. Technol. Conf.*, Montreal, QC, Canada, Sep. 2006, pp. 1–5.

[30] H. Yang, M. H. A. J. Herben, I. J. A. G. Akkermans, and P. F. M. Smulders, "Impact analysis of directional antennas and multiantenna beamformers on radio transmission," *IEEE Trans. Veh. Technol.*, vol. 57, no. 3, pp. 1695–1707, May 2008.

[31] J. G. Proakis and M. Salehi, *Digital Communications*, 5th ed., New York, NY, USA: McGraw-Hill, 2008.

[32] H. Krim and M. Viberg, "Two decades of array signal processing research: The parametric approach," *IEEE Signal Process. Mag.*, vol. 13, no. 4, pp. 67–94, Jul. 1996.

[33] H. L. Van Trees, *Optimum Array Processing: Part IV of Detection, Estimation, and Modulation Theory*. Hoboken, NJ, USA: Wiley, 2002.

[34] C. A. Balanis, *Antenna Theory: Analysis and Design*, 4th ed., Hoboken, NJ, USA: Wiley, 2016.

[35] S. Coleri, M. Ergen, A. Puri, and A. Bahai, "Channel estimation techniques based on pilot arrangement in OFDM systems," *IEEE Trans. Broadcast.*, vol. 48, no. 3, pp. 223–229, Sep. 2002.

[36] T. S. Rappaport, *Wireless Communications: Principles and Practice*, 2nd ed., Upper Saddle River, NJ, USA: Prentice-Hall, 2002.

[37] M. K. Simon and M.-S. Alouini, *Digital Communication Over Fading Channels*, 2nd ed., Hoboken, NJ, USA: Wiley, 2005.

[38] P. Stoica and R. Moses, *Spectral Analysis of Signals*. London, U.K.: Pearson, 2005.

[39] D. C. Montgomery, *Design and Analysis of Experiments*, 10th ed., Hoboken, NJ, USA: Wiley, 2020.

[40] H. Xiang, B. Chen, M. Yang, S. Xu, and Z. Li, "Improved direction-of-arrival estimation method based on LSTM neural networks with robustness to array imperfections," *Int. J. Speech Technol.*, vol. 51, no. 7, pp. 4420–4433, Jul. 2021.

[41] H. Liu, L. Zhang, Z. Chen, S. Liu, B. Liang, and Y. Deng, "Continuous DOA estimation via tensorized LSTM," in *Proc. 16th Int. Conf. Signal Process. Syst. (ICSPS)*, Mar. 2025, p. 159.

[42] Q. Li, X. Zhang, and H. Li, "Online direction of arrival estimation based on deep learning," in *Proc. IEEE Int. Conf. Acoust., Speech Signal Process. (ICASSP)*, Apr. 2018, pp. 2616–2620.

[43] P. M. Santos and L. Javier Puente Lam, "Cooperative AoA wireless positioning using LSTM neural network: Preliminary results," in *Proc. IEEE 100th Veh. Technol. Conf.*, Oct. 2024, pp. 1–5. [Online]. Available: https://pmssantos.github.io/pubs/Santos2024f_Cooperative_AoA_Wireless_Positioning_using_LSTM_Neural_Network_Preliminary_Results.pdf

[44] J. F. Lin, "Machine learning-based angle-of-arrival estimation of RF signals," Master's thesis, Dept. Elect. Comput. Eng., Univ. Massachusetts Dartmouth, Dartmouth, MA, USA, 2025. [Online]. Available: https://repository.lib.umassd.edu/view/pdfCoverPage?instCode=01MA_DM_INST&filePid=13155680190001301&download=true

[45] H. Arab, I. Ghaffari, R. M. Evina, S. O. Tatu, and S. Dufour, "A hybrid LSTM-ResNet deep neural network for noise reduction and classification of V-band receiver signals," *IEEE Access*, vol. 10, pp. 14797–14806, 2022.

[46] Z. Ke and H. Vikalo, "Real-time radio technology and modulation classification via an LSTM auto-encoder," *IEEE Trans. Wireless Commun.*, vol. 21, no. 1, pp. 370–382, Jan. 2022.

[47] S. J. Olickal and R. Jose, "LSTM projected layer neural network-based signal estimation and channel state estimator for OFDM wireless communication systems," *AIMS Electron. Electr. Eng.*, vol. 7, no. 2, pp. 187–195, 2023.

[48] B. Panda and P. Singh, "A deep convolutional-LSTM neural network for signal detection of downlink NOMA system," *AEU-Int. J. Electron. Commun.*, vol. 170, Oct. 2023, Art. no. 154797.

[49] D.-T. Nguyen, T.-H. Le, V.-S. Doan, and V.-P. Hoang, "UNet-rootMUSIC: A high accuracy direction of arrival estimation method under array imperfection," *AEU-Int. J. Electron. Commun.*, vol. 173, Jan. 2024, Art. no. 155008.

[50] Z. Du, B. Chen, X. Wang, and Y. Zhu, "Nested U-shape network for robust direction-of-arrival estimation," *IEEE Trans. Veh. Technol.*, vol. 74, no. 7, pp. 11081–11094, Jul. 2025.

[51] D. Sun, Z. Jia, T. Teng, and C. Ma, "Robust high-resolution direction-of-arrival estimation method using DenseBlock-based U-Net," *J. Acoust. Soc. Amer.*, vol. 151, no. 5, pp. 3426–3436, May 2022.

[52] X. Fu, D. Sun, and T. Teng, "A high-resolution method for direction of arrival estimation based on an improved self-attention module," *J. Acoust. Soc. Amer.*, vol. 156, no. 4, pp. 2743–2758, Oct. 2024.

[53] M. Nuhoglu and H. Cirpan, "Deep semantic segmentation for multi-source localization using angle of arrival measurements," 2025, *arXiv:2506.10107*.

[54] A. Mukherjee, R. Banerjee, and A. Ghose, "A novel u-net architecture for denoising of real-world noise corrupted phonocardiogram signal," 2023, *arXiv:2310.00216*.

[55] J. Liu, T. Wang, Y. Li, C. Li, Y. Wang, and Y. Shen, "A transformer-based signal denoising network for AoA estimation in NLoS environments," *IEEE Commun. Lett.*, vol. 26, no. 10, pp. 2336–2339, Oct. 2022.

[56] D. Lloria, S. Roger, C. Botella-Mascarell, M. Cobos, and T. Svensson, "A ResNet approach for AoA and AoD estimation in analog millimeter wave MIMO systems," in *Proc. IEEE 35th Int. Symp. Pers., Indoor Mobile Radio Commun. (PIMRC)*, Sep. 2024, pp. 1–6.

[57] N. Li, X. Zhang, F. Lv, and B. Zong, "Direction-of-arrival estimation via sparse Bayesian learning exploiting hierarchical priors with low complexity," *Sensors*, vol. 24, no. 7, p. 2336, Apr. 2024.

[58] J. Lu, Y. Yang, and L. Yang, "An efficient off-grid direction-of-arrival estimation method based on inverse-free sparse Bayesian learning," *Appl. Acoust.*, vol. 211, Aug. 2023, Art. no. 109521.

[59] C. F. Mecklenbriiuker, P. Gerstoft, and G. Leus, "Sparse Bayesian learning for DOA estimation of correlated sources," in *Proc. IEEE 10th Sensor Array Multichannel Signal Process. Workshop (SAM)*, Jul. 2018, pp. 533–537.

[60] H. Yan, T. Chen, P. Wang, L. Zhang, R. Cheng, and Y. Bai, "A direction-of-arrival estimation algorithm based on compressed sensing and density-based spatial clustering and its application in signal processing of MEMS vector hydrophone," *Sensors*, vol. 21, no. 6, p. 2191, Mar. 2021.

[61] S. E. El-Khamy, A. M. El-Shazly, and A. S. Eltrass, "A compressive sensing based computationally efficient high-resolution DOA estimation of wideband signals using generalized coprime arrays," *Wireless Pers. Commun.*, vol. 134, no. 3, pp. 1571–1597, Feb. 2024.

[62] Y. I. Abramovich and B. A. Johnson, "Expected likelihood support for deterministic maximum likelihood DOA estimation," in *Proc. IEEE Sensor Array Multichannel Signal Process. Workshop*, Oct. 2010, pp. 237–240.

[63] B. Ottersten, M. Viberg, P. Stoica, and A. Nehorai, "Exact and large sample maximum likelihood techniques for parameter estimation and detection in array processing," in *Radar Array Processing* (Springer Series in Information Sciences), S. Haykin, J. Litva, and T. J. Shepherd, Eds., Berlin, Germany: Springer, 1993, pp. 99–151, doi: 10.1007/978-3-642-77347-1_4.

[64] R. Schmidt, "Multiple emitter location and signal parameter estimation," *IEEE Trans. Antennas Propag.*, vol. AP-34, no. 3, pp. 276–280, Mar. 1986.

[65] S. Liu, X. Li, Z. Mao, P. Liu, and Y. Huang, "Model-driven deep neural network for enhanced AoA estimation using 5G gNB," in *Proc. AAAI Conf. Artif. Intell.*, Mar. 2024, vol. 38, no. 1, pp. 214–221.

[66] Y.-T. Liu, K.-C. Wang, R. Chao, S. M. Siniscalchi, P.-C. Yeh, and Y. Tsao, "MSEMG: Surface electromyography denoising with a Mamba-based efficient network," in *Proc. IEEE Int. Conf. Acoust., Speech Signal Process.*, Jun. 2025, pp. 1–5.

[67] J. Orlik, M. Krier, D. Neusius, K. Pietsch, O. Sivak, and K. Steiner, "Recent efforts in modeling and simulation of textiles," *Textiles*, vol. 1, no. 2, pp. 322–336, Aug. 2021.

[68] D. Shan, K. Zeng, W. Xiang, P. Richardson, and Y. Dong, "PHY-CRAM: Physical layer challenge-response authentication mechanism for wireless networks," *IEEE J. Sel. Areas Commun.*, vol. 31, no. 9, pp. 1817–1827, Sep. 2013.

[69] A. Boyle and M. E. Tolentino, "Localization within hostile indoor environments for emergency responders," *Sensors*, vol. 22, no. 14, p. 5134, Jul. 2022.

AHMAD ALDELEMY (Member, IEEE) received the B.Sc. degree in computer science from the University of Bradford and the master's degree (Hons.) in business analytics from Manchester Metropolitan University. He is currently pursuing the Ph.D. degree with the University of Bradford, with a focus on applying artificial intelligence in healthcare monitoring within 5G networks. He has earned several prestigious Microsoft certifications that enhance his proficiency in data analysis tools and cloud services, empowering him to manage and interpret large data sets for strategic decision-making effectively. He is actively involved in European Union research initiatives that explore cutting-edge AI applications in technology and education. As a Teaching Assistant with the University of Bradford, he has enhanced his pedagogical skills, helping to bridge the gap between theoretical knowledge and practical application in data science. Additionally, he applies his analytical expertise as a Data Analyst, ensuring data integrity and functionality across various platforms. He participates selectively in academic conferences, contributing significantly to the discourse on AI and telecommunications. His research interests include using AI in signal processing and radio frequency management, especially at the intersection of AI innovations in telecommunications. His notable early achievements include receiving the Khalifa Award for his innovative contributions to educational technology.

ALI AL-DULAIMI (Member, IEEE) received the B.Eng. and M.Sc. degrees in electronics and communications engineering from the University of Baghdad, Iraq, in 1998 and 2001, respectively, and the M.Eng. degree in quality systems engineering and the Ph.D. degree in electrical and computer engineering from Concordia University, Montreal, Canada, in 2016 and 2020, respectively.

As a Postdoctoral Research Fellow at Concordia University, he contributed to a high-impact collaborative initiative with York University, advancing AI-driven diagnostics in complex engineering systems. He served as a Lead Instructor of the Community Initiatives Support Program in Montreal, from 2018 to 2020, bridging technical excellence with societal impact. From 2022 to 2024, he led field research operations for Tiger Produce Canada and served as the Quality and Project Manager of the Berries Group, London, ON, Canada, applying data-driven quality control systems at scale. Currently, he is an Associate Professor and the Head of the School of Computing and Innovative Technologies, British University Vietnam (BUV), where he leads transformative research at the intersection of artificial intelligence, signal processing, and predictive systems engineering. His work pioneers the integration of deep learning, neural signal modeling, and adaptive AI architectures to revolutionize prognostic health management (PHM). By fusing stochastic filtering, time-series forecasting, and self-learning neural networks, he enables real-time, autonomous failure prediction in dynamic industrial systems-dramatically improving reliability, reducing downtime, and optimizing maintenance strategies across energy, manufacturing, and healthcare infrastructure. His scholarly pursuits foster a deeper understanding of predictive analytics in engineering and health management systems, including developing general-purpose theories in machine learning through advanced deep learning techniques. A thought leader in intelligent systems, his contributions are shaping the next generation of AI-augmented engineering—where data becomes wisdom, and signals become foresight.

GEILI T. A. EL SANOUSI (Member, IEEE) received the M.Sc. degree in personal mobile and satellite communications from the University of Bradford, in 2006, and the first Ph.D. degree in electrical/electronics (antenna arrays) from the University of Khartoum, in 2017. He is currently pursuing the second Ph.D. degree in design engineering with Middlesex University. He worked in several key positions in both field jobs and academic lecturing. He received the Sudanese National Prize for innovative research, in 2010, for his registered WiMax network architecture patent, in 2008.

PRINCE O. SIAW (Member, IEEE) was born in Ghana. He received the Bachelor of Science degree in medicinal chemistry in Italy and the Foundation degree in engineering and the Bachelor of Engineering degree in biomedical engineering in U.K., in 2020 and 2023, respectively. He is currently pursuing the Ph.D. degree with the University of Bradford. He was a Research Fellow with European Union's Horizon-MSCA-RISE-2019-2024, Marie Skłodowska-Curie Research and Innovation Staff Exchange (RISE) Program. His research interests include the development of radio frequency sensors for monitoring and detecting abnormalities in the bone fracture healing process. In addition to his research, he was a Teaching Assistant, participated in laboratory work, and supervised undergraduate final-year and M.Sc. students on their projects. He connected with the latest advancements and professional networks in his field. He has also contributed articles related to his area of expertise. He is an Active Member of the Institution of Mechanical Engineers (IMechE) and the Institution of Engineering and Technology (IET).

NAZAR T. ALI (Senior Member, IEEE) received the Ph.D. degree in electrical and electronic engineering from the University of Bradford, U.K., in 1990. From 1990 to 2000, he held various posts with the University of Bradford as a Researcher and a Lecturer. He worked on many collaborative research projects in U.K., under the umbrella of the Centre of Research Excellence, the Department of Trade and Industry (DTI), and EPSERC. This involved a consortium of several universities and industrial companies. He is currently an Associate Professor with Khalifa University, United Arab Emirates. He has over 100 papers published in peer-reviewed high-quality journals and conferences. His current research interests include antennas and RF circuits and systems, indoor and outdoor localization techniques, and RF measurements.

VIKTOR DOYCHINOV (Senior Member, IEEE) received the B.Eng. degree in telecommunications from the Technical University of Sofia, the M.Sc. degree in spacecraft technology and satellite communications from University College London, and the Ph.D. degree in electronic and electrical engineering from the University of Leeds. Then, he spent several years there working as a Postdoctoral Researcher with the Institute of Robotics, Autonomous Systems, and Sensing. He joined the University of Bradford as a Lecturer in electronics and software engineering, in August 2022, and a post affiliated with the Bradford-Renduchintala Centre for Space AI. He has worked on a wide range of single- and multi-disciplinary projects, all of which have involved the use of RF and wireless technology in one form or another, e.g., implantable antennas for exploratory neuroscience studies and wireless communications for infrastructure robotics. His wider skillset includes linear and non-linear design and simulation of RF/microwave circuits, components, and systems using keysight ADS and ansys HFSS among others; linear and non-linear RF measurements up to 100s of GHz, including S-parameter, modulated signal, and on-wafer probe measurements; dielectric material characterization, including soft biological tissue and custom fixture design; and the use of software-defined radio for propagation measurements and wireless communication system prototyping.

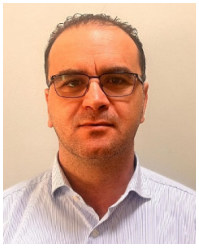

YOUSEF DAMA (Senior Member, IEEE) received the Bachelor of Science degree in electrical engineering from An-Najah National University, Palestine, in 2005, the Master of Science degree in personal mobile and satellite communications from the University of Bradford, U.K., in 2006, and the Ph.D. degree in broadband wireless systems engineering from the University of Bradford, in 2013. He is currently an Assistant Professor of telecommunications engineering with An-Najah National University. He is also the Vice Dean of the Faculty of Engineering. His recent focus involves actively participating in curriculum and course development initiatives aimed at cultivating intellectually stimulating learning environments that nurture creativity and inquisitiveness, with a particular interest in vocational education and training.

RAED A. ABD-ALHAMEED (Senior Member, IEEE) has been a Research Visitor with Wrexham University, Wales, since 2009, covering the wireless and communications research areas, and an Adjunct Professor with the College of Electronics Engineering, Ninevah University, since 2019, and the Department of Information and Communication Engineering, College of Science and Technology, University of Basrah, Basrah, Iraq. He is currently a professor of electromagnetic and radiofrequency engineering with the University of Bradford, U.K. He is also the Leader of radiofrequency, propagation, sensor design, and signal processing with the School of Engineering and Informatics, University of Bradford, where he is also leading the Communications Research Group. He is a Chartered Engineer. He has years of research experience in the areas of radio frequency, signal processing, propagation, antennas, and electromagnetic computational techniques. He is a Principal Investigator for several funded applications to EPSRCs, Innovate U.K., UKRI, DASA, British Academy, and British Council, and the Leader of several successful knowledge transfer programs, such as with Arris (previously known as Pace plc), Yorkshire Water plc, Harvard Engineering plc, IETG Ltd., Seven Technologies Group, Emkay Ltd., Two World Ltd., and SARgard Ltd. He has also been a Co-Investigator of several funded research projects, including HORIZON-MSCA-2024-SE-01-01, AeroNet: Proposal titled: "In-flight Broadband Connectivity and Experimentation for Beyond 5G Networks;" H2020-MSCA-RISE-2024-2028, Marie Skłodowska Curie, Research and Innovation Staff Exchange (RISE), titled "6G Terahertz Communications for Future Heterogeneous Wireless Network;" HORIZON-MSCA-2021-SE-01-01, Type of Action: HORIZON-TMA-MSCA-SE 2023-2027: ROBUST: Proposal titled "Ubiquitous eHealth Solution for Fracture Orthopaedic Rehabilitation;" Horizon 2020 Research and Innovation Program; H2020 MARIE Skłodowska-CURIE ACTIONS: Innovative Training Networks Secure Network Coding for Next Generation Mobile Small Cells 5G-US; European Space Agency: Satellite Network of Experts V, Work Item 2.6: Frequency selectivity in phase-only beamformed user terminal direct radiating arrays; Nonlinear and demodulation mechanisms in biological tissue (Department of Health, Mobile Telecommunications and Health Research Program); and Assessment of the Potential Direct Effects of Cellular Phones on the Nervous System (EU: collaboration with six other major research organizations across Europe). He has published more than 900 academic journals and conference papers. In addition, he has co-authored nine books and several book chapters, including seven patents. His research interests include computational methods and optimizations, wireless and mobile communications, sensor design, EMC, beam steering antennas, energy-efficient PAs, and RF pre-distorter design applications. He is a fellow of the Institution of Engineering and Technology and the Higher Education Academy. He was a recipient of the Business Innovation Award for the successful KTP with Pace and Datong companies on the design and implementation of MIMO sensor systems and antenna array design for service localizations. He has been the General Chair of the IMDC-IST International Conference, since 2020. He is the chair of several successful workshops on energy-efficient and reconfigurable transceivers: an approach toward energy conservation and CO2 reduction that addresses the biggest challenges for future wireless systems. He has been a Co-Editor of *Electronics* (MDPI), since 2019, and a Guest Editor of *IET Science, Measurement and Technology*, since 2009.